

Cite this article as:

Gurreri, L., Tamburini, A., Cipollina, A., Micale, G., Ciofalo, M., Flow and mass transfer in spacer-filled channels for reverse electro dialysis: a CFD parametrical study, *Journal of membrane science*, 497 (2016) 300-317
<http://dx.doi.org/10.1016/j.memsci.2015.09.006>

Flow and mass transfer in spacer-filled channels for reverse electro dialysis: a CFD parametrical study

L. Gurreri, A. Tamburini*, A. Cipollina, G. Micale, M. Ciofalo

*Dipartimento di Ingegneria Chimica, Gestionale, Informatica, Meccanica (DICGIM), Università di Palermo (UNIPA) –
viale delle Scienze Ed.6, 90128 Palermo, Italy.*

**e-mail: alessandro.tamburini@unipa.it*

Abstract

In Reverse ElectroDialysis (RED) concentration polarization phenomena and pressure drop affect strongly the power output obtainable; therefore the channel geometry has a crucial impact on the system optimization. Both overlapped and woven spacers are commonly commercialised and adopted for RED experiments; the latter exhibit some potential advantages, such as better mixing and lower shadow effect, but they have been poorly investigated in the literature so far.

In this work, Computational Fluid Dynamics was used to predict fluid flow and mass transfer in spacer-filled channels for RED applications. A parametric analysis for different spacer geometries was carried out: woven (*w*) and overlapped (*o*) spacers with filaments at 90° were simulated, and Reynolds number, pitch to height ratio (*l/h*) and orientation with respect to the main flow ($\alpha = 0^\circ$ and $\alpha = 45^\circ$) were made to vary.

The filament arrangement was found to be a crucial feature; for any given pumping power, higher Sherwood numbers were provided by the *w*-arrangement. The influence of flow attack angle and filament spacing depends on Reynolds number and filament arrangement. Only the configuration *w*- $\alpha 45$ avoids the presence of poorly mixed zones near the wires. Among the cases investigated here, the configuration that provided the best mixing conditions was *w*, $l/h = 2$, $\alpha = 45^\circ$.

Keywords

Reverse electro dialysis (RED); spacer-filled channel; concentration polarization; mass transfer; CFD.

1 Introduction and literature review

1.1 Introduction

Salinity gradient power is a renewable source of energy arising from the difference of chemical potential between two solutions at different concentrations. Reverse electrodialysis (RED) is a very promising technology, which converts the potential energy of a salinity gradient into electric energy by means of the controlled mixing of the two solutions, flowing in alternate channels separated by selective ion exchange membranes. The *cell pair* is the repeating unit of the stack, and contains a cationic exchange membrane, a concentrated compartment (e.g. seawater), an anionic exchange membrane and a diluted compartment (e.g. river water). An electric potential difference, due to the chemical potential difference, is established over each membrane, along with a selective transport of cations and anions from each concentrated channel towards the two adjoining diluted ones. This ionic transport is then converted in an electric current supplying an external load by means of reversible redox reactions at the electrodic compartments. More details on the physical principles and on the features of a typical RED system can be found in the literature [1-5].

Pressure drop and polarization phenomena may reduce significantly the efficiency of membrane processes. In fact, the pressure drop is responsible for an energy consumption increase, while the polarization phenomena lead to higher power consumption in non-spontaneous processes and lower driving force in spontaneous processes [6-17].

In RED, hydraulic losses reduce the net power produced, while concentration polarization, i.e. concentration gradients in the boundary layer between the membrane surface and the fluid bulk [18], decreases the gross power: the real electromotive force over the membrane is reduced with respect to the theoretical value (corresponding to the bulk concentrations), and a lower potential difference over the stack is achieved [19].

As the flow rate increases, the non-Ohmic resistances due to concentration polarization and the streamwise change of the bulk concentration are reduced and thus the gross power P_g increases asymptotically towards a maximum value P_g^{max} . On the other hand, higher flow rates lead to increased pressure drop. As a consequence of these opposite effects, the net power density P_n has a maximum value P_n^{max} at an optimal flow rate of the feed solutions which depends on the specific configuration of the stack [5, 17, 19-24]. The reduction in power output due to the pumping power P_p (i.e., P_p/P_g) reported in the literature amounts normally to ~10-20% at the flow rate that maximizes the net power. The loss of power with respect to the maximum (asymptotic) value of gross power $(P_g^{max} - P_n^{max})/P_n^{max}$ is much higher; this parameter quantifies the loss with respect to the theoretical maximum achievable, and, from literature data, can be estimated to be ~25-45% [5, 19, 22-25].

The channel configuration is a prominent feature of a RED stack for fluid dynamics and mass transfer, as it affects the flow and the concentration fields within the channel and thus determines distributed pressure drop and concentration polarization. Optimal flow rate and channel configuration should be identified as a compromise solution taking into account different aspects.

In this regard, net spacers in either flat sheet or spiral wound modules represent an essential element of RED stacks and many other membrane processes as electrodialysis, reverse osmosis, ultra-filtration, nano-filtration, membrane distillation, etc. A spacer consists of a net of polymeric filaments and can be made with different geometrical features. For example, commercial net spacers can be made of either woven or overlapped wires. Spacers are adopted as mechanical support for the membranes, giving dimensional stability to the channel, but they can also promote fluid mixing thus reducing polarization phenomena. On the other hand, they exhibit the drawback of increased pressure drop, as well as higher electrical resistance (an important feature in RED) and reduced active membrane area due to shadow effects [2, 17, 19, 23, 26]. Therefore the channel geometry optimization

must take into account mechanical stability, mass transfer (mixing), hydraulic friction and electrical resistance.

1.2 Literature review

Several studies can be found in the literature on the characterization of spacer-filled channels, aimed at investigating the effect of spacer geometry (filament spacing, filament diameter, filament arrangement, angle between crossing filaments, flow attack angle) on fluid dynamics features such as flow pattern, recirculation, shear rate distribution, flow regime, pressure drops and mass transport phenomena.

Isaacson and Sonin [27] carried out limiting current measurements in an six-channel electro dialyzer (one cell pair, two guard channels and the two electrodic compartments) in order to investigate the spacer performance. Correlations for the Sherwood number (Sh) and the friction factor (f) as functions of the Reynolds number (Re) were found for eddy promoters consisting of cylindrical rods placed in the center of the channel with axes perpendicular to the flow direction. The optimal spacing was about four times channel thickness, and exhibited performance comparable with traditional spacers.

Tanaka [28] performed similar limiting current density measurements on anion and cation exchange membranes in a six-channel electro dialyzer. A diamond spacer with overlapped filaments was used in the measuring channel. Results showed that the adopted spacer did not increase the limiting current density, probably because of the dead spaces between the spacer and the membrane; thus a spacer might well have no positive effects on mixing enhancement.

Balster et al. [29] tested the performance of different spacer configurations by limiting current density measurements in a six-compartment electro dialysis stack. Conventional non-woven, modified, twisted, and multi-layer spacers were tested. The presence of a spacer clearly enhanced mass transfer with respect to the empty channel. Results showed that twisted rectangular filaments

can provide better mixing than round filaments due to swirling flows, although the channel performance is also affected by the angle between filaments and the flow attack angle. At the same power number (Pn , proportional to fRe^3), which expresses in non-dimensional form the power consumption per unit volume, the best multi-layer spacer tested showed a 20% increment in mass transfer with respect to a conventional spacer.

Schock and Miquel [30] carried out tests of some commercial spacers, collecting experimental data on pressure drop and mass transfer in spiral wound modules for pressure driven processes. Correlations among the aforementioned dimensionless numbers were obtained, and a performance calculation aiming at optimizing spiral wound elements was addressed.

Da Costa et al. [31] analysed in more detail the spacer characteristics developing a semi-empirical model which permits the evaluation of spacer performance (specifically for ultrafiltration). For the case of main flow bisecting the angle between the filaments, this angle was found to be the most important parameter and the value of 90° was found to be the best compromise between high mass transfer coefficients and low pressure drop.

In the study of spacer-filled channels for membrane processes, computational fluid dynamics (CFD) is a very effective method for a detailed analysis at small scale and for testing a number of different cases.

Schwinge et al. examined flow [32] and mass transfer [33] for cylindrical spacer filaments that were oriented orthogonally to the main flow direction, by two-dimensional CFD modelling.

Karode and Kumar [34] applied 3D CFD simulation to several commercial spacers for evaluating pressure drop and the average shear exerted by the fluid on the walls.

Li et al. [35] carried out 3D CFD simulations to determine mass transfer coefficients and power consumption of net spacers. The geometric parameters investigated were the mesh length, the angle between the filaments and the flow attack angle. The optimal spacer geometry was that characterized

by a ratio of filament spacing to channel height of 4, the angle between filaments of 120° and the flow direction bisecting this angle. The same authors validated experimentally these simulations in a subsequent paper [36], obtaining mass transfer coefficients by the limiting current method. This latter paper reports also some experimental results for woven spacers which, to the authors' knowledge, are the only data for such spacers reported in the literature.

Ranade and Kumar [37] showed that a “unit cell” approach can be successfully used in CFD simulations, allowing small-scale flow features to be resolved in detail. Also, the contributions of form drag and viscous drag to the overall pressure drop were quantified and spacers with different cross-sections were studied.

Santos et al. [38] investigated spacers made of rectangular cross-section filaments by means of (i) direct numerical simulations (DNS) on periodic cells and (ii) experiments, finding that all the fluid flow features were mainly determined by the transverse filaments, while the longitudinal filaments had no significant effect.

Koutsou et al. [39] carried out DNS in a periodic unit cell and experimental tests on diamond spacers, by changing the filament spacing and the angle between the crossing filaments (β). As expected, pressure drop tends to decrease by increasing the filament spacing and by reducing β . The same authors published a systematic study (CFD simulations and experiments by limiting current) on mass transfer [40]. Lower values of Sh were obtained as the filament spacing increased, and as β decreased. Also the dependence of Sh on the Schmidt number (Sc) was studied, finding a power law with exponent near 0.4, as in turbulent channel flow.

Shakaib et al. [41] studied different spacers, in some of which the transverse and longitudinal filaments were of different diameters. They analysed by CFD the effects of spacer geometry (spacing and thickness of the two sets of filaments, flow attack angle and angle between the filaments) on pressure drop and shear stress. The same authors investigated also mass transfer [42]. A comparison

between shear stress distribution and mass transfer coefficient distribution was done. The average mass transfer coefficient was found to increase in (i) spacers with increased transverse filament thickness and (ii) spacers with higher angle between filaments which cause a zigzag nature of the flow.

For the sake of completeness, it should be mentioned that further papers have been devoted to unsteady flow regimes [43, 44], others have been focused on multi-layer or non-conventional spacers [29, 45-49] and others yet have addressed the CFD modelling of pressure driven membrane processes [50-52] or of membrane distillation [53, 54].

From this review, it can be argued that the literature is still lacking in some fields: (a) the investigation of spacers made by woven filaments. This type of spacers is commercially available and commonly used in the experimental campaigns for RED applications [4, 5, 22, 23, 55, 56] and can offer some potential benefits, such as a better mixing and a lower shadow effect. (b) very low Reynolds numbers. Typical RED channels are very thin ($< 500 \mu\text{m}$), and usual flow velocity in these channels are not more than a few cm/s. This means that, as a difference from other membrane processes, RED is characterized by very low Re which are not properly investigated in the literature.

In this work, 3D-CFD simulations have been carried out, predicting fluid flow and mass transfer in channels with woven and non-woven spacers for RED applications. The specific aim is to provide important insights on the channel geometry optimization in the range of Re of highest interest for RED by means of the characterization of spacers, including some that have poorly investigated so far.

2 CFD modelling

The CFD simulations reported in this work are based on the modelling presented in an earlier paper [2]. Therefore, only the main aspects are summarized here.

2.1 Systems under investigation

A net spacer can be made by a variety of geometries on the basis of: filament shape/arrangement, angle between crossing filaments, number of layers, filament spacing, filament size. Other features as deformability and wettability are related to the material. Also, fluid dynamics and mass transfer within a spacer-filled channel depend strongly on the flow attack angle, i.e. the relative orientation of the spacer with respect to the main flow direction.

The cases investigated in this work regard diamond-type spacers characterized by filaments of circular cross-section crossing orthogonally and presenting the same diameter d and spacing l . In regards to the wire arrangement, both woven and non-woven (overlapped) spacers are simulated. In this paper, the channel height h was kept fixed and three different values of l were simulated, corresponding to: $l/h = 2, 3, 4$. These values fall within the range expected in most industrial applications of membrane processes and are those most commonly studied in the literature, thus allowing a comparison between the present simulation results and data from published work. Two different flow attack angles (α) were investigated: the flow direction is either parallel to a filament ($\alpha = 0^\circ$) or bisects the angle formed by the filaments ($\alpha = 45^\circ$). Figure 1a shows an example of real spacers with overlapped and woven wires crossing at 90° , indicating also the filament spacing l and the main flow direction. The parametric analysis was carried out for four values of the Reynolds number (see definition in section 2.4): $Re = 1, 4, 16, 64$. This represents quite a wide range, since typical values of Re for RED stacks are $\sim 1-10$; for a channel $300 \mu\text{m}$ thick this range corresponds to superficial velocities of $0.15-1.5 \text{ cm/s}$. All cases investigated are reported in Table 1. For convenience, each case studied is identified by a code where the first letter indicates the overlapped (o) or woven (w) arrangement of filaments, and l/h and α are followed by their respective values.

In the overlapped case with $\alpha = 0^\circ$, the vertical plane parallel to the main flow direction is a geometric symmetry plane. For all other channel configurations, this is a geometric antisymmetry plane. These features are reflected on the flow and concentration fields.

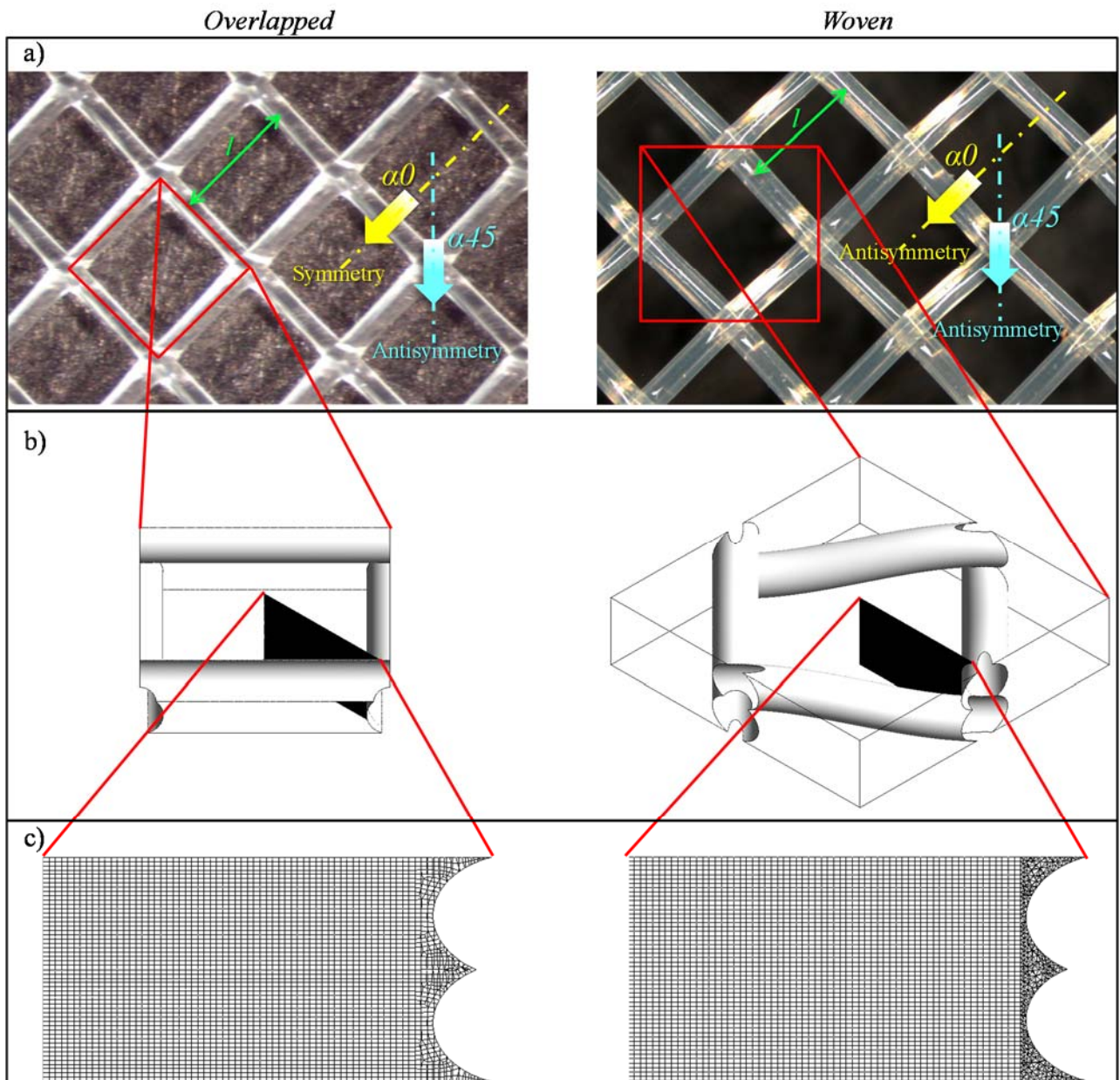


Figure 1. Spacer geometries investigated. Left: overlapped; right: woven. (a) arrows indicate the different flow directions with respect to the spacer, lines indicate the projection of the symmetry and antisymmetry planes; (b) Unit Cell geometry; (c) details of the mesh over one half of a cross section of the Unit Cell.

Table 1. Cases investigated.

Case/code	Filaments arrangement	l/h [mm]	α [°]	Re [-]
<i>o-l/h2-α0</i>	overlapped	2	0	
<i>o-l/h3-α0</i>	overlapped	3	0	
<i>o-l/h4-α0</i>	overlapped	4	0	
<i>o-l/h2-α45</i>	overlapped	2	45	
<i>o-l/h3-α45</i>	overlapped	3	45	
<i>o-l/h4-α45</i>	overlapped	4	45	1, 4, 16, 64
<i>w-l/h2-α0</i>	woven	2	0	
<i>w-l/h3-α0</i>	woven	3	0	
<i>w-l/h4-α0</i>	woven	4	0	
<i>w-l/h2-α45</i>	woven	2	45	
<i>w-l/h3-α45</i>	woven	3	45	
<i>w-l/h4-α45</i>	woven	4	45	

In commercial spacers either a compenetration or a deformation of filaments can be observed in the proximity of the contact areas, depending on the manufacturing technique; similarly, the filaments will also be compressed to some degree in the contact areas with the membranes when the spacers are employed in an assembled stack. These aspects were taken into account during the generation of the geometries, as discussed in [2], by assuming $(2d-h)/2d = 10\%$; 70% of this quantity was attributed to the overlap region of the filaments, while 30% to the filament-membrane contacts. These values were obtained via optical microscopy from measurements of commercial spacers (some of them are simulated in [2]) and from data by Da Costa et al. [31].

The fluid simulated is a NaCl aqueous solution at a concentration of 0.5 M, typical of seawater, at 25 °C. The physical properties of the solution are [57-59]: density $\rho = 1017 \text{ kg/m}^3$, dynamic viscosity $\mu = 9.31 \cdot 10^{-4} \text{ Pa s}$, diffusivity of NaCl in water $D = 1.472 \cdot 10^{-9} \text{ m}^2/\text{s}$. Seawater is usually employed as the concentrated solution (coupled with river water as the diluted one), but it can also be fed as the diluate coupled with brine, as proposed within the EU-FP7 funded REAPower project [60-63].

In this study, the influence of the Schmidt number on mass transfer is not assessed. However, in the case of NaCl solutions this dependence seems not to be important. In fact, the Schmidt numbers for river water (0.017 M), seawater (0.5 M) and brine (5.0 M) are $Sc = 583, 622, 888$ respectively [57-59]; moreover, the Sherwood number is a weak function of Sc for the low Reynolds numbers considered here [64]. Therefore the Sherwood number depends very little on the specific electrolyte concentration considered.

2.2 Governing equations

The computational domain consists of a repetitive periodic unit of the channel (Unit Cell); therefore the governing equations have to be adapted to a periodic domain. Assuming a Newtonian incompressible fluid, the steady-state continuity and momentum transport (Navier-Stokes) equations for three-dimensional flow in a periodic cell are:

$$\vec{\nabla} \cdot \vec{u} = 0 \quad (1)$$

$$\rho \vec{u} \vec{\nabla} \cdot \vec{u} = -\vec{\nabla} \tilde{p} + \mu \nabla^2 \vec{u} + \vec{P} \quad (2)$$

where \vec{u} is velocity, ρ is density, μ is dynamic viscosity, \tilde{p} is the periodic component of pressure (whose spatial distribution repeats itself identically in each Unit Cell) and \vec{P} is a body force per unit volume representing the large-scale component of the driving pressure gradient along the main flow direction (chosen here to be coincident with the z axis) [2, 65].

The choice of steady-state simulations deserves a comment. We performed a relatively accurate transition study only for the woven configuration and $l/h = 2$. Using the definition of the Reynolds number adopted in the present paper, we found steady-state flow up to $Re = 314$ ($\alpha = 0/90^\circ$) or 273 ($\alpha = 45^\circ$), periodic flow for $Re = 352$ ($\alpha = 0/90^\circ$) or 365 ($\alpha = 45^\circ$) and chaotic (turbulent) flow for $Re \geq 390$ ($\alpha = 0/90^\circ$) or 466 ($\alpha = 45^\circ$).

For the overlapped geometry, we have not yet performed a study focused on transition to turbulence. However, for $l/h = 2$ we found steady state flow at $Re = 336$ ($\alpha = 0/90^\circ$) or 316 ($\alpha = 45^\circ$), turbulent flow for $Re \geq 595$ ($\alpha = 0/90^\circ$) or 523 ($\alpha = 45^\circ$). For $l/h=4$, at $\alpha = 0/90^\circ$ we found steady state flow at $Re = 226$ ($\alpha = 0/90^\circ$) or 217 ($\alpha = 45^\circ$), unsteady flow for $Re \geq 330$ ($\alpha = 0/90^\circ$) or 312 ($\alpha = 45^\circ$).

For overlapped spacers characterized by $l/h = 3-6$ and flow attack angle $\alpha = 45^\circ$, Koutsou et al. [39] report the onset of the first flow instabilities at Reynolds numbers of 140-180 (according to the definition adopted in the present paper). Thus, some discrepancy with our results exists since, under comparable conditions, e.g. $l/h = 4$, we obtained steady flow up to $Re \approx 217$. This difference may partly be explained by the different grid resolution adopted in the present study ($\sim 2 \times 10^6$ volumes, 99% of which hexahedra) and in the cited reference ($\sim 3 \times 10^5$ volumes).

From the rigorous Stefan-Maxwell equation under the assumptions of (i) binary electrolyte and (ii) local electroneutrality, a transport equation, valid also for concentrated solutions, was obtained [2]

$$\vec{\nabla}(\tilde{C}\vec{u}) = \vec{\nabla}(D_{corr}\vec{\nabla}\tilde{C}) - K_c w \quad (3)$$

where

$$D_{corr} = D \frac{b}{b + (a - M_e)(\tilde{C} + K_c z)} \quad (4)$$

In Eqs. (3) and (4) D is the diffusion coefficient of the electrolyte, a and b are the linear regression parameters of the function $\rho = \rho(C)$ [57], M_e is the molar mass of the electrolyte, w is the local value of the velocity component along the main fluid flow direction z , and K_c is the large-scale concentration gradient along z . The quantity \tilde{C} in Eq. (3) is the periodic component of the concentration, such that its spatial distribution repeats itself identically in each Unit Cell. It is introduced in order to impose

periodic boundary conditions, notwithstanding the streamwise variation of the bulk concentration due to the wall flux, and is defined as

$$\tilde{C}(x, y, z) = C(x, y, z) - K_c z \quad (5)$$

The large-scale gradient K_c is

$$K_c = \frac{\bar{J}_{IEM}^d \cdot S}{w_{ave} \cdot V} \quad (6)$$

in which \bar{J}_{IEM}^d is the mean value of the electrolyte flux entering the channel at the walls (imposed in the simulation), S is the membrane surface area in a unit cell, w_{ave} is the volume-averaged velocity along z in the unit cell and V is the unit cell volume. Note that the transport equation (Eq. (3)) is solved for \tilde{C} ; the real (non periodic) concentration C can be inferred from Eq. (5).

Eq. (3) is as a convection-diffusion equation, with a weak non-linearity in the diffusive term and an additional source term $-K_c w$. Note that the migrative term does not explicitly appears in Eq. (3) because the divergence of the migrative flux is negligible compared to the divergence of the diffusive one and thus does not affect the concentration field. Migrative fluxes themselves are not assumed to be negligible, but are simply superimposed on the diffusive ones without affecting them and are reflected in the boundary conditions of Eq. (3) [2].

2.3 Computational domain and boundary conditions

A single channel was simulated, and an incoming electrolyte flux was imposed through the walls representing the membrane-solution interfaces; therefore, the computational domain represents the dilute channel. The membranes and all phenomena occurring at molecular scale in the electric double layer were not included in the computational domain and thus were not explicitly modelled, but are implicitly accounted for in the boundary conditions.

Several CFD studies of spacer-filled channels based on the above Unit cell approach can be found in the literature [2, 35, 37-41, 65-68]. This treatment is justified by the fact that the fully developed fields are attained after just a few unit cells [36, 42]. Figure 1b shows examples of the Unit Cells adopted for the two kind of spacer-filled channels simulated in the present work. The choice of the cell size and orientation with respect to the spacer wires is arbitrary for spacers with crossing filaments of equal diameter [67]; therefore, in both spacer-filled channels the minimum periodic unit is chosen. In the case of overlapped wires the choice is also suggested by the possibility of building up an almost completely hexahedral grid. The computational domains were created on the basis of the geometric features and the assumptions on the compenetration/compression of filaments in their contact areas and in the contact areas with the walls, as described in section 2.1.

The computational domain for the overlapped configuration was discretized by multi-block grids composed almost entirely by hexahedral elements (less than 1% of the domain volume was meshed by tetrahedra, pyramids and wedges, see Table 2). For the woven configuration, multi-block hybrid grids, although mainly composed by hexahedral elements, had to be created, due to the geometrical complexities. In particular, the zones around the filaments were discretized by tetrahedra, while the remaining part of the computational domain was discretized with hexahedral volumes (see Table 2); pyramids and wedges were necessary at the interfaces between the two parts. In general, hexahedral or hybrid grids provide a greater accuracy and a better convergence to grid-independent results with respect to fully tetrahedral grids [65].

An analysis of the results' sensitivity to the computational grid was performed. Various grids were tested for the case of the highest Re investigated and the results obtained were compared, including global quantities (averages on the whole domain) and trends of local quantities on lines perpendicular to the walls. The results show that both velocities and concentrations vary by less than 1% when the number of grid nodes in the wall normal direction increases beyond ~ 40 . Therefore, a mesh size

corresponding to 51 control volumes in the channel height was chosen for the final simulations. The grids used contain a number of finite volumes ranging from $\sim 4 \cdot 10^5$ to $\sim 6 \cdot 10^6$ depending on the specific geometry simulated. The number of finite volumes increases with l/h , and is higher for the woven spacer-filled channels both because the domain volume is twice larger and because it is partly discretized with tetrahedra. Figure 1c reports enlarged details of the meshes in one half of a cross section (at 45° with respect to the filaments). The mesh features are summarized in Table 2.

Table 2. Summary of the grids employed.

Unit Cell	Number of finite volumes in height h	Number of finite volumes	% of domain volume discretized with hexahedra
$o-l/h2$	51	421'042	>99
$o-l/h3$		1'050'986	>99
$o-l/h4$		1'922'001	>99
$w-l/h2$		1'657'319	66.3
$w-l/h3$		3'397'154	77.2
$w-l/h4$		5'756'552	82.8

Translational periodicity conditions were imposed on the lateral boundaries of the domain. In each case, the Unit Cell was oriented with respect to the reference frame $Oxyz$, so that the main flow direction coincided with the z axis. The Unit Cells shown in Figure 1b are oriented so that the flow attack angle is $\alpha = 45^\circ$. The body force per unit volume \vec{P} in Eq. (2) was set in order to achieve the desired Re (1, 4, 16, 64) on the basis of preliminary simulations. All the other boundaries representing fluid-solid interfaces (fluid-membrane and fluid-filament) are set as walls with no-slip conditions and a Neumann boundary condition for the concentration: a uniform flux is imposed at the upper and lower walls, while the flux is set to zero at the fluid-filament interfaces.

Under the assumption of ideal membranes (permselectivity equal to 100%) and transport numbers of ions in the solution equal to 0.5, the diffusive flux at the membranes J_{IEM}^d can be correlated to the current density i [2] as

$$J_{IEM}^d = \frac{i \cdot 0.5}{F} \quad (7)$$

where F is the Faraday constant. A uniform current density was imposed, as in the previous paper [2].

The functional dependence of D_{corr} on the concentration is weak. Also, the variation of the concentration within the domain is relatively limited, due to the low electrolyte fluxes usually involved. For these reasons, the diffusivity varies less than 1%. Since the non-linearity of the transport equation (3) is so weak [2], the Sherwood number is practically independent of the current density; therefore simulating different values of i is not necessary.

2.4 Definitions

The hydraulic diameter of the channel is assumed equal to twice the channel thickness, as in the case of an empty (spacer-less) channel of infinite streamwise and spanwise extent

$$d_{h,void} = 2h \quad (8)$$

The Reynolds number was calculated in accordance with

$$Re = \frac{\rho w_{mean,void} d_{h,void}}{\mu} \quad (9)$$

where $w_{mean,void}$ is the average velocity along the main flow direction z in a corresponding spacer-less channel, i.e. the superficial velocity as in previous studies [27, 39, 40]. The Fanning friction factor is defined as

$$f = \frac{\Delta p}{\Delta z} \frac{d_{h,void}}{2\rho w_{mean,void}^2} \quad (10)$$

where $\Delta p/\Delta z$ is the mean pressure gradient along the main flow direction and coincides with the module of the source term \bar{P} in Eq. (2). The pumping power consumption is evaluated by means of the dimensionless power number, defined as [35]

$$Pn = \text{SPC} \frac{\rho^2 h^4}{\mu^3} = \frac{1}{8} f Re^3 \quad (11)$$

where SPC is the specific power consumption per unit volume in the corresponding void channel

$$\text{SPC} = \frac{\Delta p}{\Delta z} w_{\text{mean,void}} \quad (12)$$

The local and average mass transfer coefficients are calculated as

$$k = \frac{J_{IEM}^d}{C_w - \hat{C}_b} \quad (13)$$

$$\bar{k} = \frac{J_{IEM}^d}{\bar{C}_w - \hat{C}_b} \quad (14)$$

where C_w and \bar{C}_w are the local and averaged wall concentration, and \hat{C}_b is the bulk concentration defined as the mass flow weighted average of the concentration on a cross section of the Unit Cell perpendicular to the main flow direction (i.e., a x - y plane on the basis of the present assumptions). Note that \bar{k} is not the surface average of k . The above definition of \bar{k} is preferable to that based on the wall average of k , because the local k may diverge at some points making this average meaningless.

The local mass transfer coefficient k can be expressed in dimensionless form as a local Sherwood number

$$Sh = \frac{k d_{h,void}}{D_{corr,ave}} \quad (15)$$

where $D_{corr,ave}$ is the volume average of the diffusivity D_{corr} in Eq. (4). Similarly, an average Sherwood number can be defined as

$$\bar{Sh} = \frac{\bar{k} d_{h,void}}{D_{corr,ave}} \quad (16)$$

Note that \overline{Sh} is not the surface average of Sh . From dimensional analysis one has that the friction coefficient f and the power number Pn depend on the Reynolds number Re and the geometry of the domain; the Sherwood number \overline{Sh} depends also on the physical properties of the solution as synthesized by the Schmidt number Sc :

$$f, Pn = f, Pn(Re, geometry) \quad (17)$$

$$\overline{Sh} = \overline{Sh}(Re, geometry, Sc) \quad (18)$$

In the parametric analysis presented in this work the dependence of \overline{Sh} on Sc is not studied, as mentioned in section 2.1; therefore, by expanding the geometry-related parameters investigated here, one has

$$f, Pn, \overline{Sh} = f, Pn, \overline{Sh}(Re, arrangement, l/h, \alpha) \quad (19)$$

in which “arrangement” means either overlapped or woven.

2.5 Computational details

The governing equations (Eqs. (1), (2), (3)) were discretized and solved in the computational domain with the boundary conditions described in section 2.3 by means of the finite volumes code Ansys[®]-CFX 14. Zero velocity and a homogeneous value of the periodic concentration (0.5 M) were imposed as the initial guess. The *High Resolution* scheme was used for the advection term discretization. A coupled algorithm was adopted to solve for pressure and velocity. All simulations were run in double precision. The convergence was assumed attained by the criteria of stabilized values of variables at monitor points and normalized residuals lower than 10^{-10} . A different number of iterations was required, depending on the features of the case simulated.

3 Results and discussion

Simulation results will now be presented and discussed. Section 3.1 reports results relevant to fluid flow, section 3.2 focuses on pressure drop, section 3.3 is devoted to mass transfer, and, finally, section 3.4 compares the present results with CFD and experimental data from the literature. For the sake of brevity, detailed results such as streamlines and Sh maps are shown only for some of the test cases simulated, in order to highlight the effect of some parameters in specific configurations, while the global variables Re , f , Pn and \overline{Sh} are reported for all the cases investigated. Each case is identified by the code reported in Table 1.

3.1 Fluid flow

The influence of the Reynolds number is shown in Figure 2, which reports in-plane streamlines in the vertical midplane parallel to the flow (see inset) for the case $o-l/h3-\alpha0$ at different values of Re . Colours indicate the normalized modulus of the velocity, $u_{norm} = |\vec{u}|/w_{ave}$. Streamlines enter the Unit Cell from below a transverse filament, then fill the whole height of the channel and finally exit the cell from below the subsequent transverse wire. At low Re (1, 4) the presence of creeping flow conditions can be observed, as the flow field is almost symmetric between upstream and downstream with almost no flow separation from the filaments. At higher Re (16, 64) the symmetry feature disappears and flow detachment downstream of the filaments occurs. Below the upper wall, in the proximity of the transverse wires, the streamlines are characterized by stagnation areas at all Re ; only at the highest Re (64) a large recirculation cell develops downstream of the transverse filaments, and the straight tract of the streamlines is shortened, i.e. the relative importance of the vertical velocity component increases. Figure 2 refers to the intermediate filament spacing investigated ($l/h = 3$) and shows that at $Re = 64$ the vortex fills almost 50% of the upper half of the cell. For $l/h = 2$, the vortex

fills the whole upper half of the cell, while, for $l/h = 4$, its streamwise extent is only $\sim 1/4^{\text{th}}$ of the cell length. The relevant maps are not shown here for the sake of brevity.

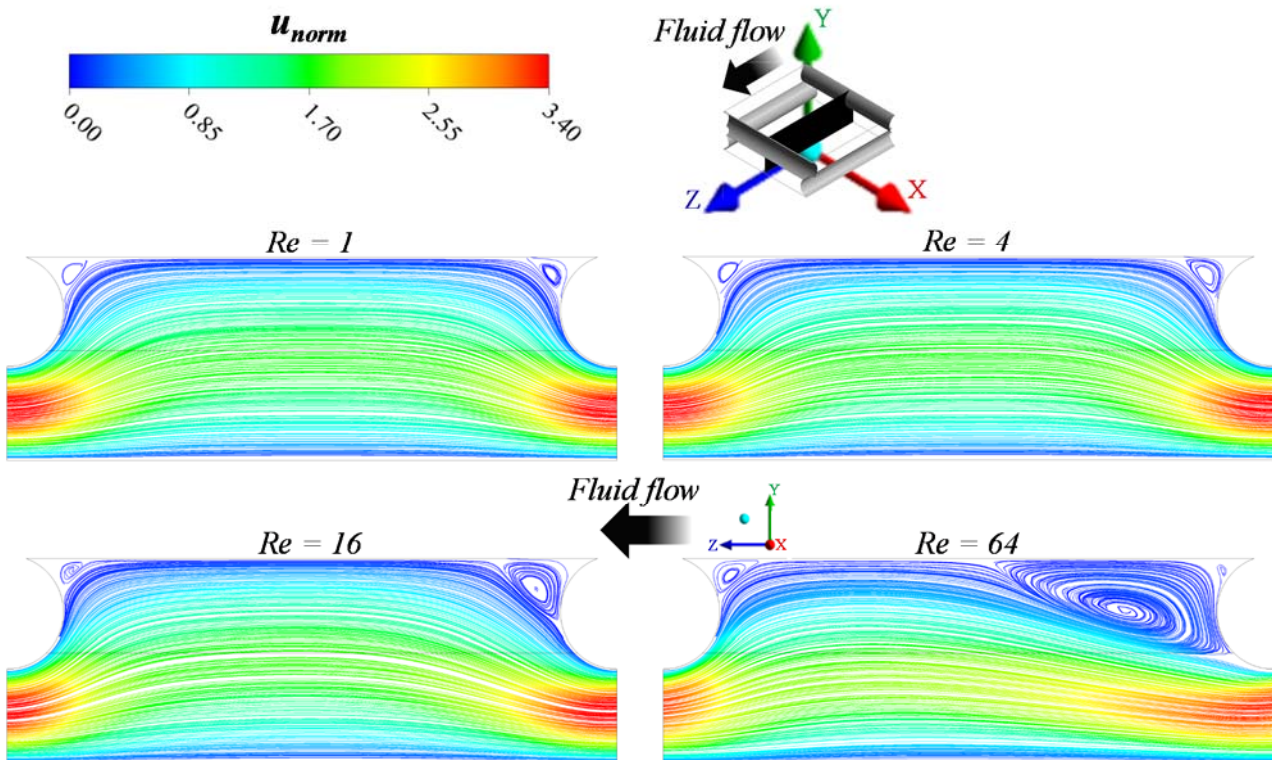


Figure 2. Streamlines on the y - z midplane for $o-l/h3-a0$ at $Re = 1, 4, 16, 64$.

Figure 3 shows the influence of the l/h ratio on the mixing performance of the spacer. It reports 3D streamlines for the same filament arrangement and the other flow attack angle (case $o-\alpha 45$), at $Re = 4$ and increasing values of l/h . Streamlines starting from the two periodic inlet faces are distinguished by two different colours. As they cross the periodic domain, the fluid threads are divided: some of them remain confined in the same half-channel (upper or lower) where they entered the unit cell, while others switch to the opposite half-channel. The fate of a fluid thread depends mainly on the spanwise location of its entrance point. For the lowest value of l/h about one half of the fluid entering the cell remains in its own half-channel, while for higher values of l/h , an increasing

part of the fluid switches to the opposite half-channel. These results confirm previous literature findings based on CFD [34, 41].

The influence of the flow rate on the streamlines pattern is shown in Figure 4, which reports 3D streamlines for case $o-l/h4-\alpha45$, at two values of Re (48 and 90), both much higher than those in Figure 3 but still in the steady-state range. For clarity purposes, only streamlines starting from one of the two periodic inlet faces are shown. It can be observed that, as Re increases, more and more of the streamlines entering the cell close to the upper filament which is located upstream with respect to the main flow direction (to the left in the figure) (i) remain in the upper half of the channel and (ii) follow a spiralling path around an approximately straight axis. The former feature confirms the effect of Re reported by Shakaib et al. [41]; the latter one, lacking in the low- Re cases in Figure 3, is similar to what reported by Koutsou et al. [39] for relatively high Reynolds numbers.

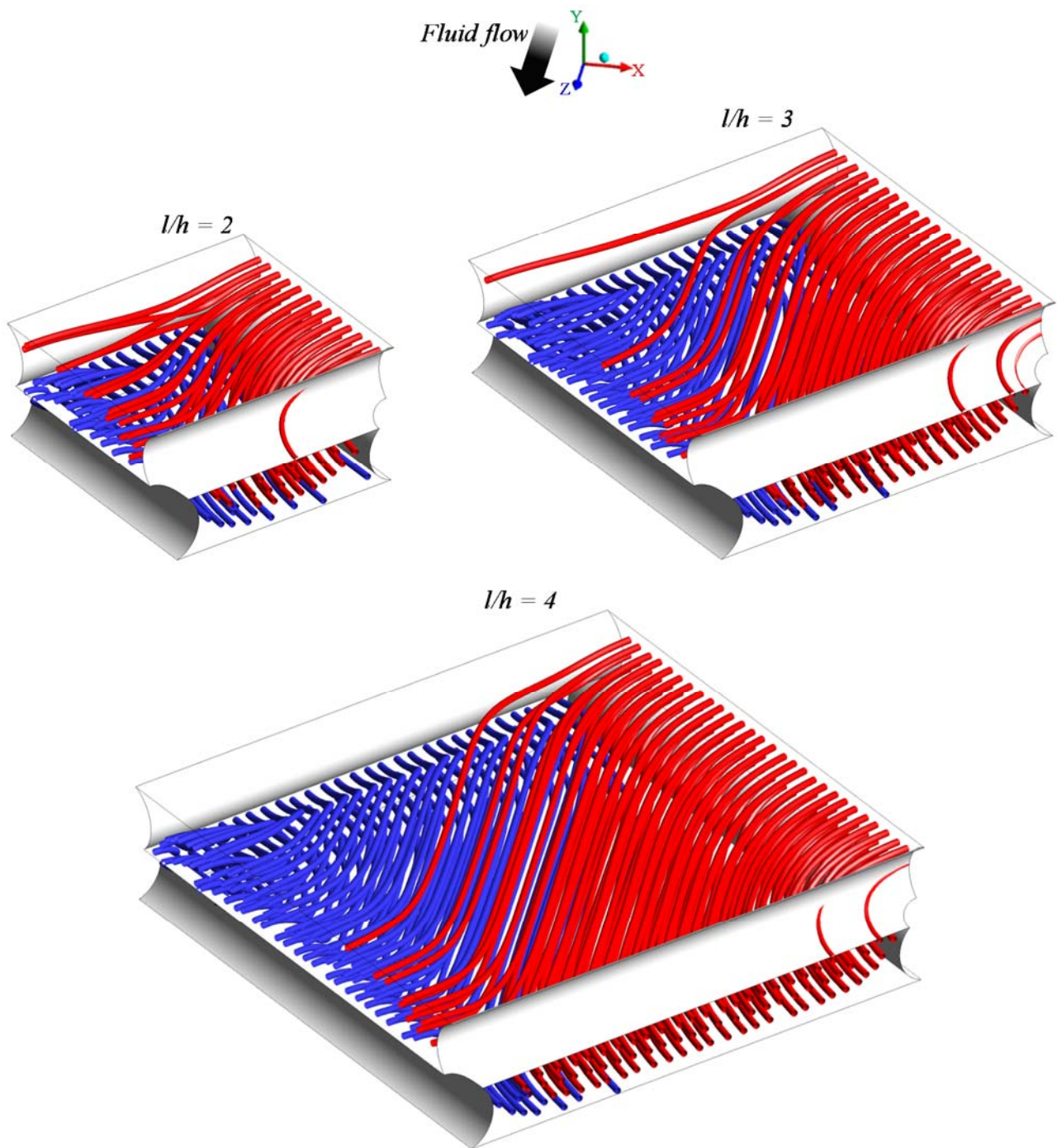


Figure 3. Streamlines for $\alpha = 45$ at $Re = 4$ at $l/h = 2, 3, 4$.

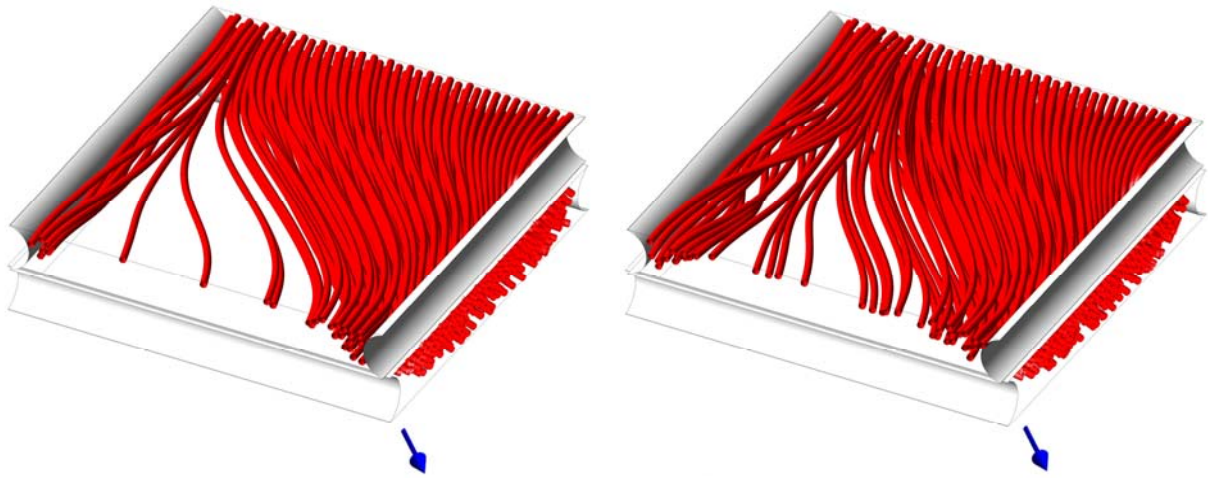


Figure 4. Streamlines for $o-l/h4-a45$ at $Re = 48$ (left) and 90 (right). Arrows indicate the main flow direction.

Figure 5 and Figure 6 correspond to Figure 2 and Figure 3, but are for the case of a woven spacer. A markedly different flow field is established in this case. In particular, Figure 5 reports streamlines for the case $w-l/h3-a0$ at increasing Re . As a difference with Figure 2, 3-D streamlines are shown due to the geometric complexity of the woven configuration. The streamlines start from a vertical plane orthogonal to the flow and cutting a transverse filament, and are represented in different colours according to whether they start from above or below the filament. Along the longitudinal wires, calm regions exist where the fluid flows slowly parallel to them. In the whole remaining part of the channel the fluid trajectories are determined by the curvilinear transversal filaments arranged alternately. If a fluid thread moving along the main flow direction encounters a larger passage area in the upper half of the channel when it crosses a transverse wire, then the same thread will encounter a larger area in the lower half at the next transverse wire, and *vice versa*. Therefore, the fluid threads located centrally and in the smaller passage area along the spanwise direction tend to remain either in the upper or in the lower half of the channel throughout the cell, while the fluid close to the longitudinal filaments flows alternately above and below the transverse ones. All streamlines exhibit very little spanwise displacement. Very small differences can be observed between different Re . When the obstacles are

farther apart (i.e. l/h is higher), the curvature of the trajectories is reduced and their rectilinear tracts become longer (figure not shown for brevity).

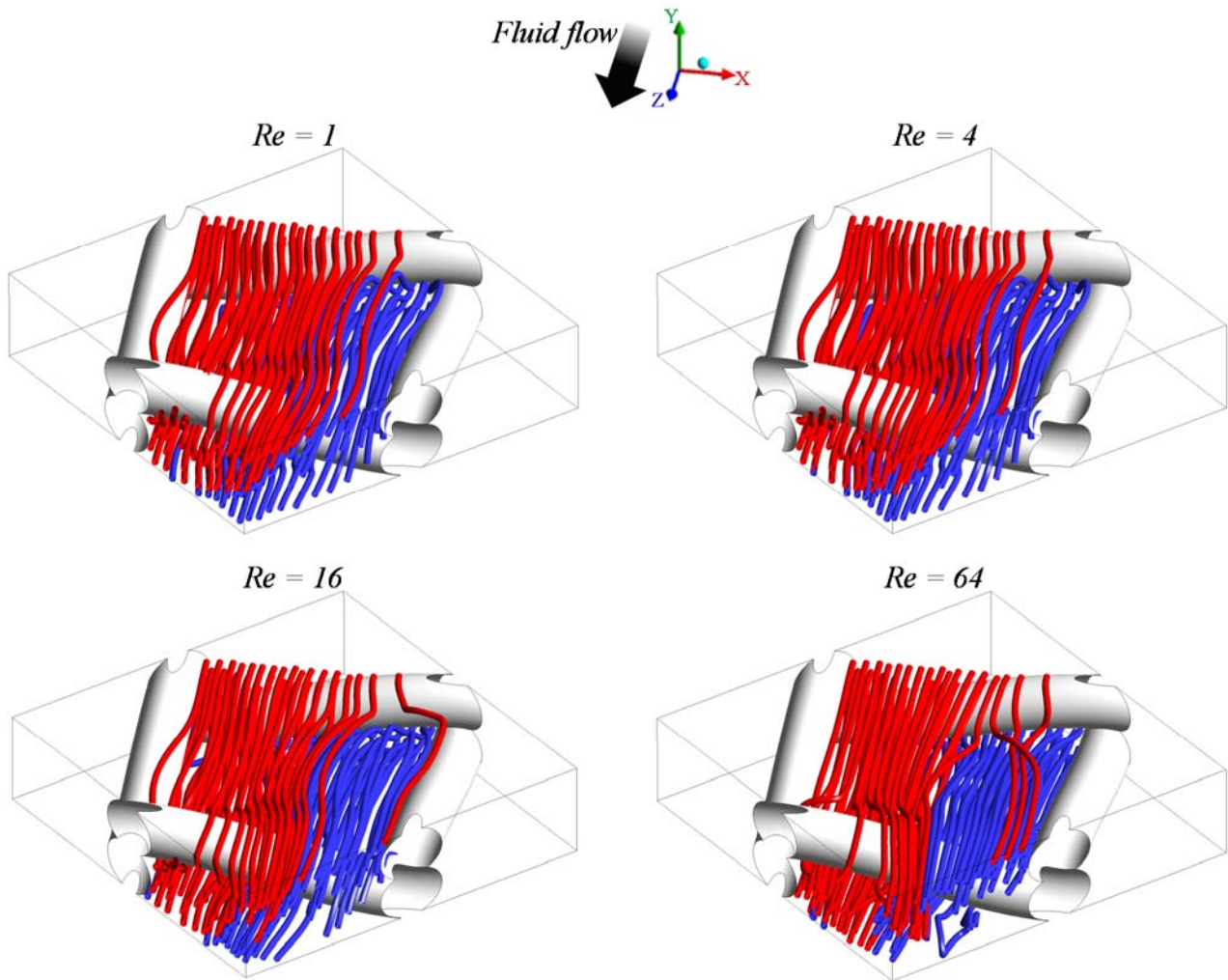


Figure 5. Streamlines for $w-l/h3-a0$ at $Re = 1, 4, 16, 64$.

When the flow attack angle is made to change (case $w-a45$) the woven filaments arrangement and their orientation with respect to the main flow direction are such as to give rise to the most complex flow field among the cases investigated here. In Figure 6 the streamlines start from two vertical planes at 45° with the main flow direction, and are visualized in four colours depending on the area from which they start. This configuration is the only one without any stagnant regions, and it forces the

fluid to move along intricate trajectories with both vertical and lateral displacements. This flow pattern is suitable for achieving a high mixing degree. As l/h increases, the streamlines become less curved, thus a lower mixing is observed. Increasing Re causes the straight tract of the streamlines to become shorter, and the streamlines to follow less the filament boundaries (not shown for brevity).

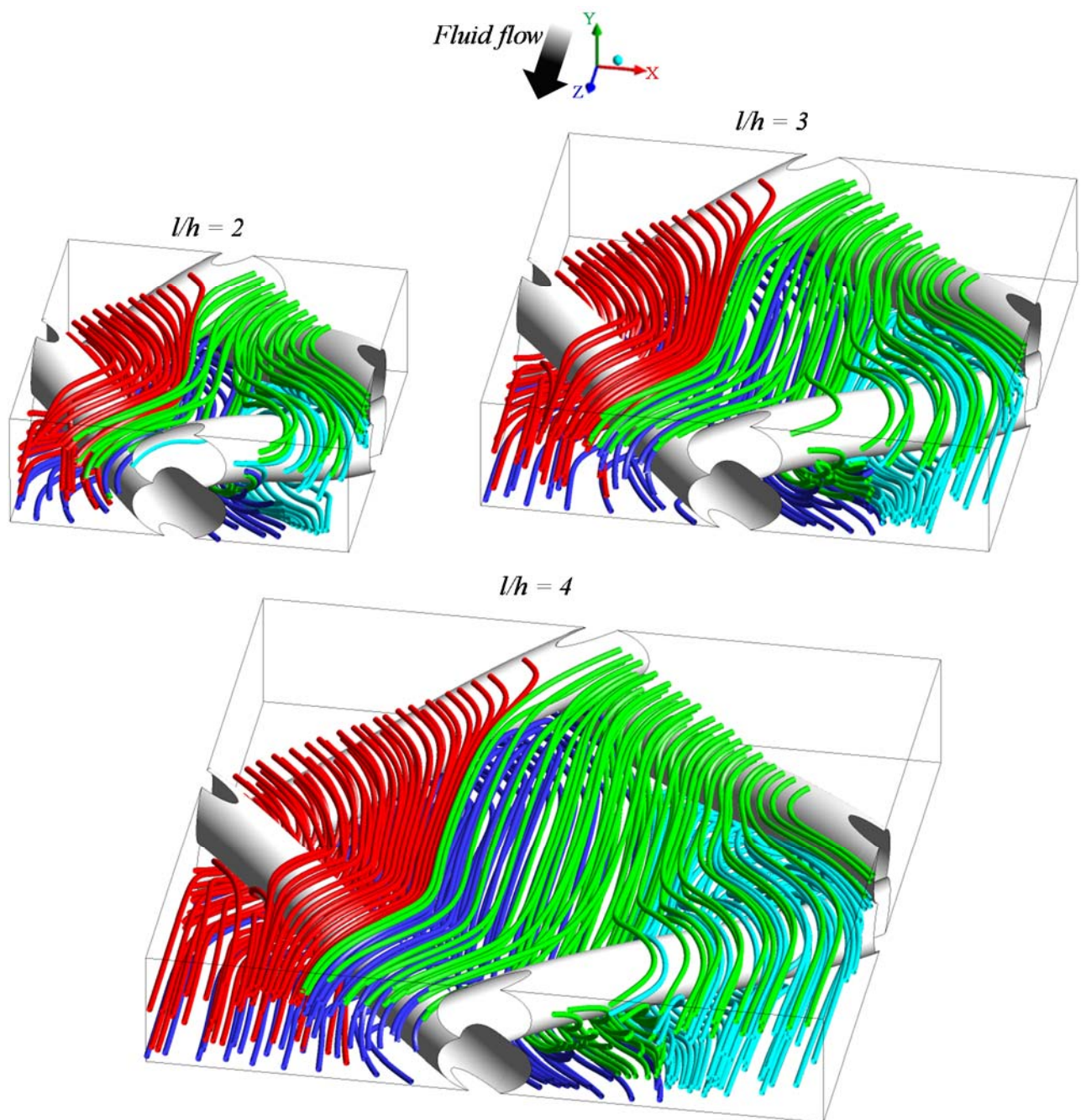


Figure 6. Streamlines for $w-\alpha45$ at $Re = 4$ at $l/h = 2, 3, 4$.

The effect of the investigated parameters on the flow field can be summarized as follows. In general, the presence of a spacer causes velocity components perpendicular to the main flow direction whose relative importance increases as the Reynolds number increases. The streamlines become more curved on the average as l/h decreases. The filament arrangement (woven *vs.* overlapped) causes completely different flow fields for both values of α investigated, but woven spacers guarantee a better mixing with respect to overlapped ones. For the overlapped arrangement, the two flow attack angles generate very different flow fields: in both cases ($o-\alpha 0$ and $o-\alpha 45$) the fluid accomplishes movements in the two directions perpendicular to the main flow direction; but in the case $o-\alpha 0$ the lateral motion is confined inside the unit cell by the side filaments parallel to the main flow direction, while in the case $o-\alpha 45$ some fluid threads follow the filament direction and thus remain in their half-channel (upper or lower), while some move towards the opposite half-channel along zigzag flow paths, with a predominance of the former when l/h decreases and Re increases. For channels with woven filaments the common features are that the flow particles move both up and down and laterally, and that the streamlines present a rectilinear tract at low Re and high l/h . On the other hand, changing α results in some important differences: the case $w-\alpha 45$ is characterized by more displacement in the lateral direction and by the absence of stagnant areas. This is a prominent feature, which makes the case $w-\alpha 45$ the most promising configuration for mixing.

3.2 Pressure drop

The Fanning friction factor is reported as a function of the Reynolds number for all the cases investigated in Figure 7. For the empty channel, one has $f = 24Re^{-1}$. For each geometry the results in Figure 7 can be expressed as

$$f = ARe^n \quad (20)$$

in which, as a first approximation, $n = -1$. In a more detailed analysis, the value $n = -1$ holds only at the lowest Re indicating a creeping (self-similar) flow regime. As Re increases, the exponent n of Re deviates slightly from -1. This is due to the slight but increasing inertial effects induced by the spacers: secondary flow appears and the overall flow field loses self-similarity as Re increases. No unsteadiness occurs in the range of Re investigated here.

The power number defined by Eq. (11) can be approximated by a power law as

$$Pn = BRe^m \quad (21)$$

where $B = A/8$ and $m = 3 + n \approx 2$. Charts of Pn vs. Re are not shown for the sake of brevity. Table 3 reports the constant A in Eq. (20), evaluated for $Re \rightarrow 0$, for all the channel configurations.

In order to better compare quantitatively the cases investigated, the charts in Figure 8 show f normalized with respect to that in an empty channel ($24/Re$). Of course, this quantity represents also Pn normalized with respect to that in an empty channel ($3Re^2$). The spacer-filled channels exhibit significant increments (3-20 times) of pressure drops with respect to the spacer-less channel. Also, these increments become higher as Re increases.

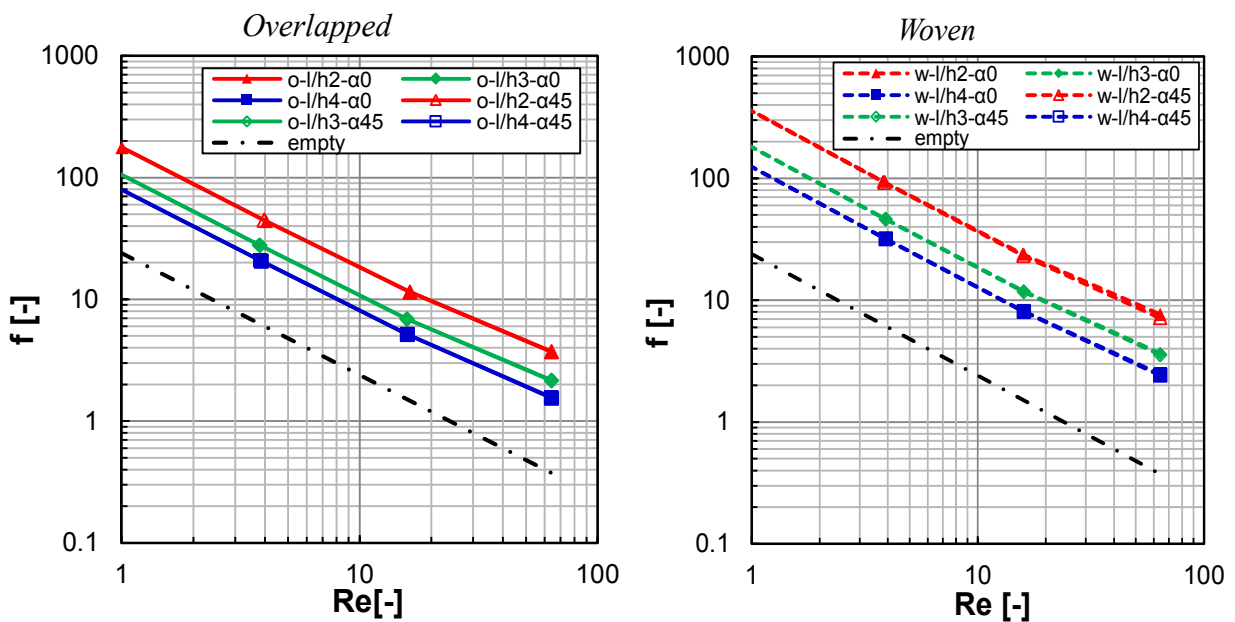


Figure 7. Friction factor as a function of Reynolds number for all cases simulated.

Table 3. Constant A in Eq. (20) for $Re \rightarrow 0$.

o/w	l/h	α	A for $Re \rightarrow 0$ [-]
<i>o</i>	2	0	177.3
<i>o</i>	3	0	105.6
<i>o</i>	4	0	79.6
<i>o</i>	2	45	177.4
<i>o</i>	3	45	105.7
<i>o</i>	4	45	79.6
<i>w</i>	2	0	358.1
<i>w</i>	3	0	180.4
<i>w</i>	4	0	124.2
<i>w</i>	2	45	356.1
<i>w</i>	3	45	179.7
<i>w</i>	4	45	123.9

The flow attack angle α effect is irrelevant at these Re [2], despite it influences deeply the flow field. The only exception is the case of the woven arrangement along with the minimum filament spacing ($w-l/h2$), which reveals a small effect of α at the highest Re .

The filament spacing l/h has remarkable effects, especially for the w -arrangement. Of course, as l/h increases, pressure drop is reduced and approaches that of the empty channel. Figure 8 reports also the percent relative increment of pressure loss and pumping power from $l/h4$ to $l/h3$ and from $l/h4$ to $l/h2$. It is evident that l/h is a crucial parameter in determining the pumping power consumption.

Also the filaments arrangement has a significant influence. The w -arrangement requires a pressure drop larger on average by 106%, 67% and 54% with respect to the o -arrangement, for $l/h = 2, 3, 4$ respectively. Thus, it is worth noting that (i) passing from overlapped to woven filaments, the

hydraulic loss increases dramatically, and (ii) the arrangement has a larger influence as the pitch to height ratio decreases.

The effect of the filament arrangement is not surprising. In fact, woven wires offer a larger fluid-solid interface for friction. Moreover, they allow the fluid to flow both above and below the obstacle, while overlapped ones significantly interact with the fluid only by one side. Finally, the components of velocity orthogonal to the main flow direction are more important, thus increasing mixing but also near wall velocity gradients and thus friction.

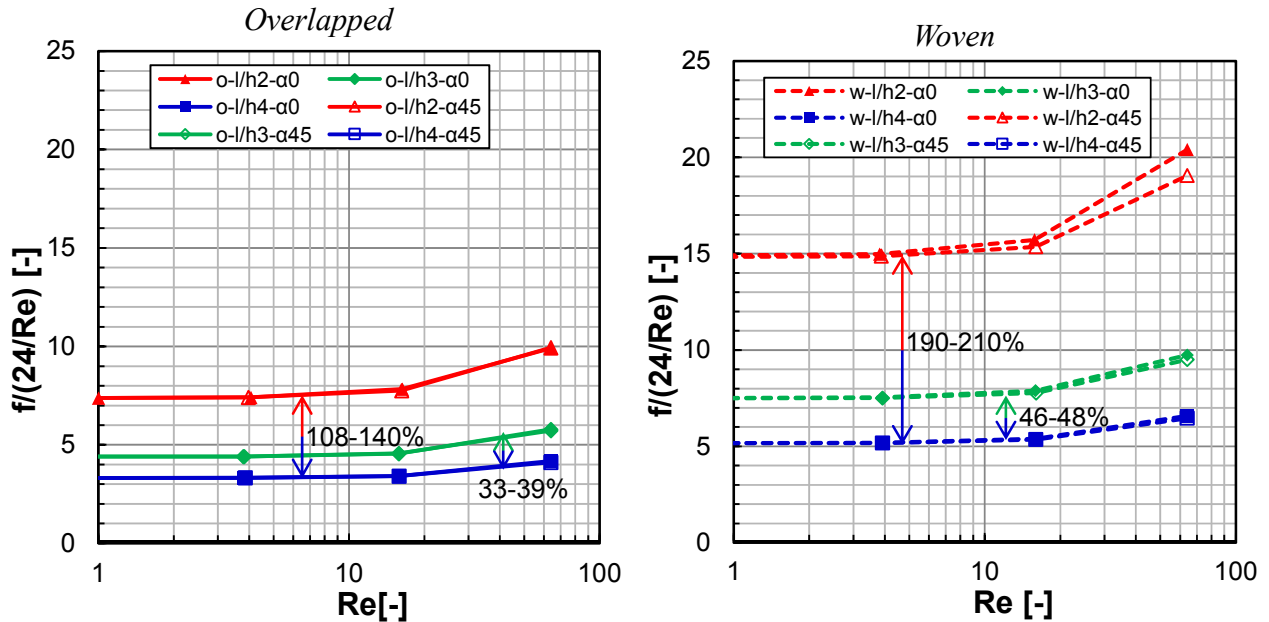


Figure 8. Friction factor normalized by that pertaining to an empty channel ($24/Re$) as a function of the Reynolds number for all cases simulated. Note that this quantity is also the power number normalized by that of the empty channel.

3.3 Mass transfer

All the simulations in this paper are run by imposing the bulk concentration \hat{C}_b and the mass flux at the walls (coinciding with the diffusive component J_{IEM}^d since there is no convection at the walls).

Since $J_{IEM}^d = D \partial C / \partial y$, where D is diffusivity, C is concentration and y is the coordinate normal to the

wall, this implies that the near-wall slope of the C profile is the same in all cases, while the concentration at the walls C_w is computed as a result of the simulation. The effect of Reynolds number and spacer configuration is to alter the C profile in the whole channel, thus affecting the wall-to-bulk concentration difference. Since the local mass transfer coefficient is defined as $k = J_{IEM}^d / (C_w - \hat{C}_b)$, an increase, say, of the Reynolds number causes a reduction of $C_w - \hat{C}_b$ and thus an increase in k (i.e., in the Sherwood number).

As an example of these effects see Figure 9 in one of our previous papers [2], which compares the wall-to-wall concentration profiles computed along a straight cross-stream line for a woven spacer and increasing Re .

3.3.1 Influence of filaments arrangement and flow attack angle

In Figure 9 the distribution of the normalized local Sherwood number on the walls is reported for different filaments arrangements and flow attack angles at a fixed value of l/h (3) and Re (4). For each case, the maps for both walls are shown from the same viewpoint. Of course, the symmetry/antisymmetry features of the geometry hold also for the concentration field. Therefore the maps on the upper and lower walls are exactly antisymmetric (i.e. are identical apart from reflections and rotations) for all cases, apart from $o-\alpha 0$: in this case each of the two maps is symmetric about the main flow direction, but the two maps differ from each other. The same scale was used for all configurations in order to make comparisons easier.

Figure 9 shows that the spacer filaments arrangement and the spacer orientation have a strong impact on the Sh distribution. Note the presence of areas with low values of Sh (thus high concentration polarization) in correspondence of calm regions with low fluid velocities near the filaments. These areas, detrimental for mixing, are located in the proximity of the longitudinal wires for the case $w-\alpha 0$ and near both filament layers for the overlapped spacer ($o-\alpha 0$ and $o-\alpha 45$). The

configuration $w-\alpha45$ is the only one able to avoid this disadvantageous effect of the filaments. This feature, combined with a complex flow field with significant convective motions orthogonal to the walls, favours mixing thus giving rise to the highest \overline{Sh} for the case $w-\alpha45$.

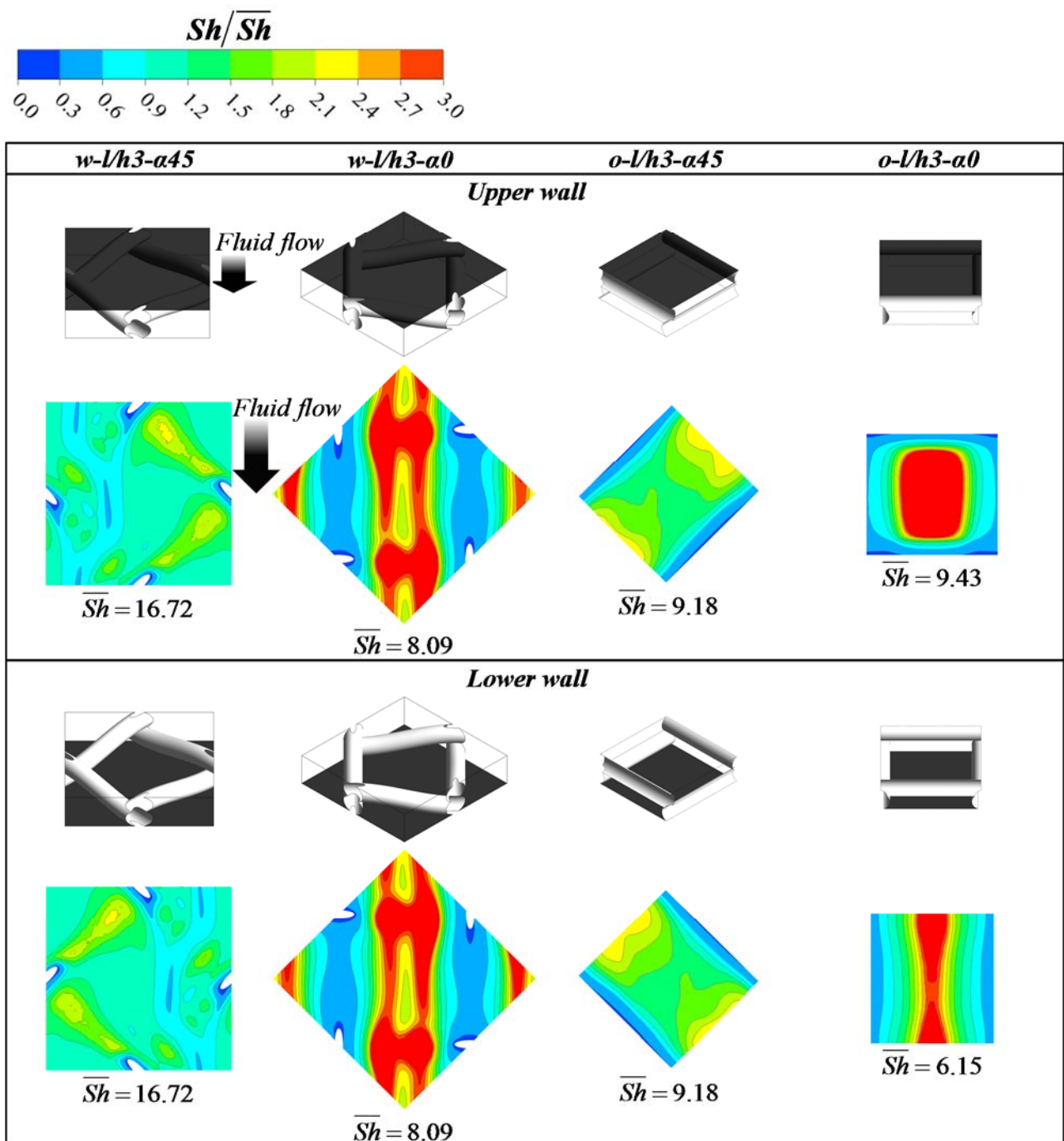


Figure 9. Maps of the normalized local Sherwood number on the upper and lower walls for the two filaments arrangement (o and w) and the two flow attack angles ($\alpha 0$ and $\alpha 45$) at $l/h=3$ and $Re = 4$.

3.3.2 Influence of Reynolds number and pitch to height ratio

Figure 10 reports the distribution of the normalized local Sherwood number on the upper wall for the case $w-\alpha 45$ by varying Re and l/h . In particular, the configuration chosen is that which offers the best performance, as it was discussed above. To make comparisons easier, the scale is the same for all cases and is also the same as that adopted in the previous Figure 9.

The maps reported in the figure are similar in shape, thus indicating that the two parameters analysed here affect the distribution of the Sherwood number less than w / o and α ; in fact, similar location of minima and maxima can be observed among the various cases of Figure 10. On the other hand, the Sh distribution is less homogeneous as \overline{Sh} increases. As expected, as Re increases, a mixing enhancement is obtained, i.e. \overline{Sh} increases, due to the increasing convective motions orthogonal to the walls. However, \overline{Sh} increases only as $\sim Re^{0.5}$. Figure 10 shows also that an increase of \overline{Sh} is obtained as the pitch decreases. This effect confirms what was inferred from the analysis of the flow field (e.g. streamlines in Figure 6).

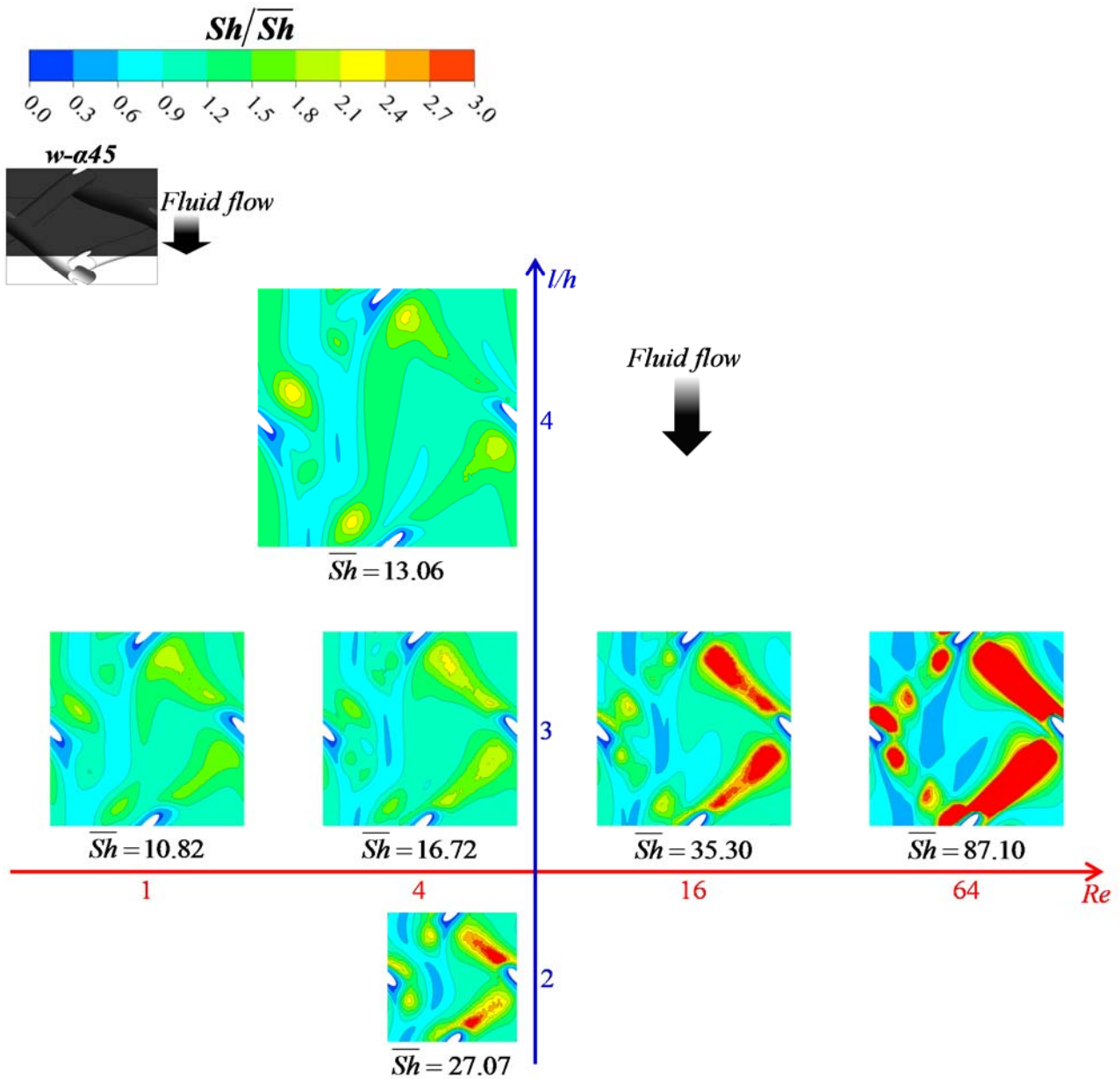


Figure 10. Maps of the normalized local Sherwood number on the upper wall for the case $w-\alpha45$ by varying Re and l/h .

Figure 11 reports \overline{Sh} as a function of Re for all cases simulated. The charts show also \overline{Sh} for fully developed laminar flow within an empty channel of infinite streamwise and spanwise extension with uniform mass flux at the walls ($\overline{Sh} \approx 8.23$). It is evident that the presence of a spacer strongly affects mass transfer phenomena. At very low Re , mixing is not favoured in the spacer-filled channels, due to the calm regions caused by the filaments which are detrimental for mass transfer, especially for $\alpha 0$.

As a consequence, the spacer-filled channels can exhibit \overline{Sh} even lower than the empty channel as also observed for different cases by Fimbres-Weihs and Wiley [69]. On the other hand, as Re increases, much higher \overline{Sh} values are attained; in fact increased inertial fluid flow phenomena come into play, thus causing a mixing enhancement. Each channel configuration is characterized by a specific cut-off value of Re beyond which mass transfer performance is better than that of the empty channel. In the case $w-\alpha45$ this occurs at Re close to 0, in the other cases at higher values, but always at Re lower than ~ 7 .

In regards to the influence of the parameters, the filament spacing has a clear effect for all Re only in the case $w-\alpha45$: in particular, \overline{Sh} decreases as l/h increases. For $w-\alpha0$ this occurs only at the highest Reynolds numbers; for the o -arrangement the dependence of \overline{Sh} on l/h is not significant.

The flow attack angle plays an important role in determining mass transfer for the w -arrangement, although it has very slight effects on pressure drop: for all Re and l/h , a mixing promotion is achieved when the fluid bisects the angle between crossing filaments, i.e. the configuration $w-\alpha45$ exhibits \overline{Sh} higher than $w-\alpha0$. On the other hand, the discrepancies between the Sherwood numbers obtained for the two values of α in woven spacer-filled channels are lower at high Re . For the o -arrangement, the effect of α is small and varies with Re .

The filament arrangement is shown to be a key parameter for mass transport. Results show that the w -arrangement allows a mixing enhancement (higher \overline{Sh}) with respect to the o -arrangement, with the exception of very low Re and $\alpha = 0$. For any given Re the configuration that guarantees the best mixing conditions is $w-l/h2-\alpha45$.

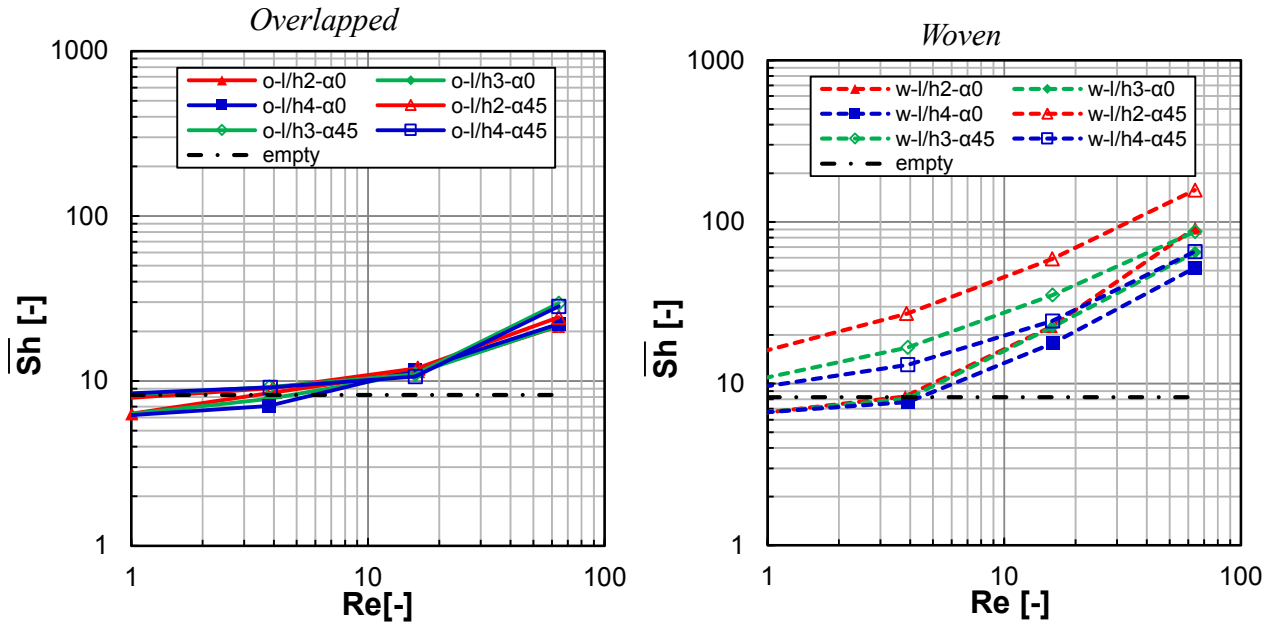


Figure 11. Sherwood number as a function of the Reynolds number for all cases simulated.

As was mentioned in discussing Figure 9, among the various configurations investigated, those characterized by overlapped filaments and attack angle of 0° (configurations $o-\alpha 0$) exhibit different distributions of the mass transfer coefficient on the two walls. In this regard, Figure 12 reports separated values of \overline{Sh} on the upper and lower walls for the $o-\alpha 0$ cases simulated (overall averages have been reported in Figure 11 left). With respect to the main flow direction, the upper wall touches the transverse filaments and the lower wall touches the longitudinal filaments. Apart from the lowest Re investigated, the flow pattern within the channel enhances mass transport at the upper wall rather than at the lower wall (see streamlines in Figure 2). Interestingly, the trend of \overline{Sh} for a given wall is not monotonic either with Re or with l/h , although the values of \overline{Sh} averaged between upper and lower walls behave more regularly, being monotonically with Re and little dependent on l/h .

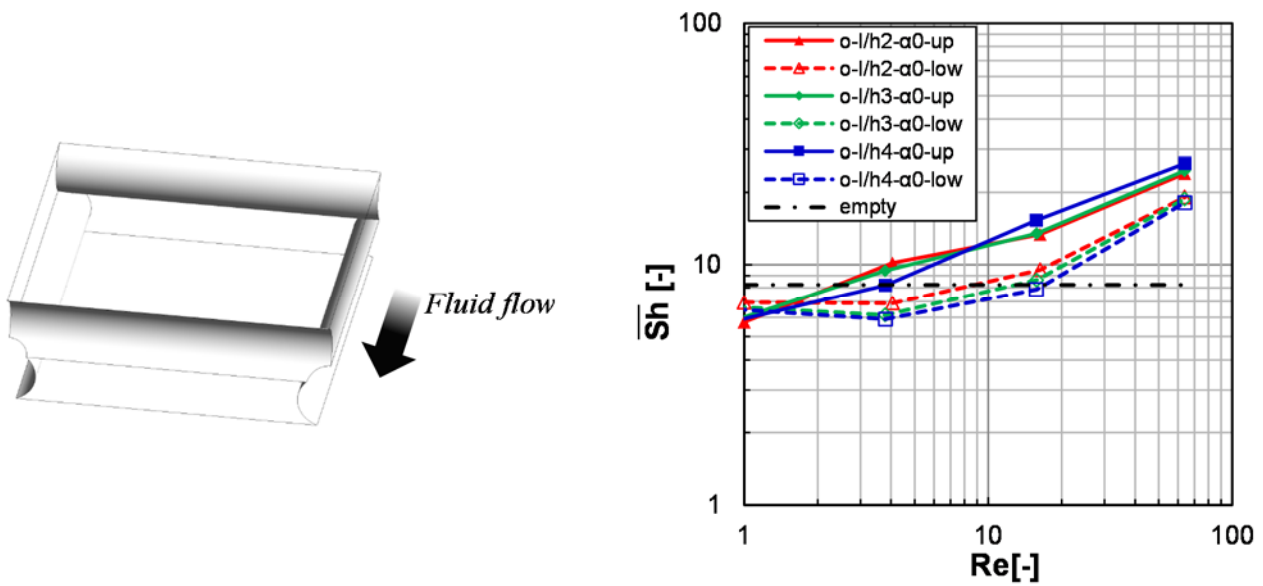


Figure 12. Separate values of the Sherwood number on the walls as functions of the Reynolds number for the $o-\alpha\theta$ cases simulated.

Figure 13 shows \overline{Sh} as a function of the power number Pn defined in Eq. (11) for all cases simulated; thus it summarizes the combined effect of all the parameters investigated on pressure drop and mass transfer. By comparing these data with those reported in Figure 11, similar considerations on the spacers performance can be inferred, although the ranking of the various cases with respect to l/h changes slightly. Figure 13 confirms the configuration $w-l/h2-\alpha45$ as that providing the best mass transfer performance not only for any given flow rate but also for any given specific pumping power consumption. Actually, the identification of the best channel configuration in a RED stack should take into account also other parameters affecting the net producible power.

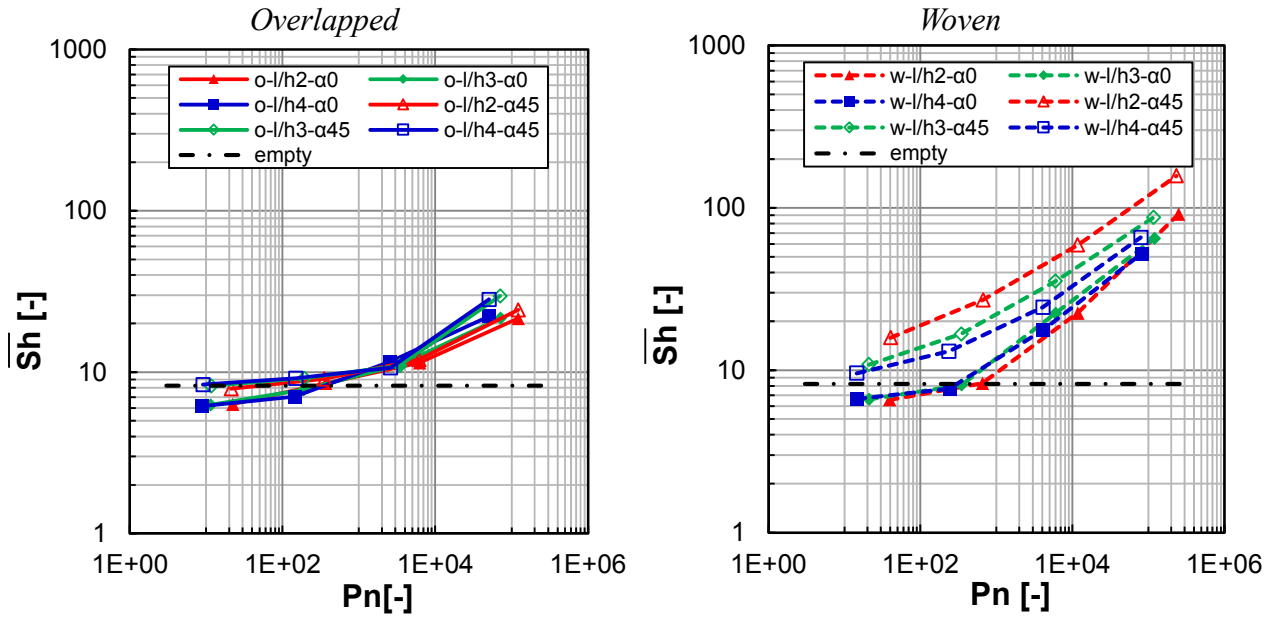


Figure 13. Sherwood number as a function of the Power number for all cases simulated.

3.4 Comparison with CFD and experimental data from the literature

Literature data show, in general, a qualitative mutual agreement for friction and mass transfer, but with non-negligible discrepancies among different authors and between numerical and experimental results. For example, the simulation results of Koutsou et al. [39] overestimate the hydraulic friction with respect to the experimental results by the same authors; moreover, similar discrepancies are found with respect to the experimental data of Schock and Miquel [30], and higher discrepancies are observable with the results by Da Costa et al. [31] and Li et al. [36]. CFD results on pressure drop by Shakaib et al. [41] are found in fair agreement with the DNS data by Koutsou et al. [39] and in even better agreement with the experiments of Li et al. [36]. Several differences are detected also for mass transfer. For example, Koutsou et al. [40] derived different correlations from experiments and CFD simulations, with (i) an overestimation of Sh numbers and (ii) a different dependence of Sh on Pn and Re with respect to literature data by Schock and Miquel [30] and Li et al. [36]. Moreover, Shakaib et al. [42] found CFD results on the Sherwood numbers with differences within 30% with respect to the experimental data by Li et al. [36].

As seen in section 3.2, the $f-Re$ and $Pn-Re$ curves can be fitted with good approximation in the range of Re investigated here by means of the typical power laws adopted in the literature. On the other hand, the effect of Re on Sh is more complex for all geometries. The $\overline{Sh}-Re$ and $\overline{Sh}-Pn$ correlations are often reported in the general literature on spacer-filled channels in the form of power laws [30, 31, 40], but these functions are not suitable for the present results, probably due to the lower range of Re investigated here [27, 35, 36, 69]. In fact, since our results include very low Reynolds numbers, the curves in Figure 11 and Figure 13 exhibit the constant- \overline{Sh} behaviour typical of creeping flow at the lower end of the Re range and tend to the power-law behaviour typical of convection-dominated flow only at the upper end of the Re range, thus inevitably exhibiting a curvature at intermediate Re even if plotted in a *log-log* chart.

Detailed comparisons with literature data are shown in the next charts of this section. For pressure drop only, in addition to the results shown so far, further CFD data obtained by our group, at higher Re (but, however, in the steady regime) are reported. In order to facilitate comparisons, the present results were converted according to the definitions adopted by the various authors cited.

First, the present results are compared with CFD and experimental data by Li et al. [35, 36]. The conditions studied by these authors are different in several respects from those of the present work: the filament diameter is exactly equal to half the channel height ($d = h/2$), the Schmidt number is 1278, and the boundary condition at the walls is $C_w = 0$. Moreover, the average mass transfer coefficient is calculated as the mean value of the local k rather than by Eq. (14). No details are provided by the authors on the computational grids adopted in their CFD simulations.

In Figure 14 the present results for Pn relative to two overlapped spacers are compared with data from [35] and [36]. Besides a qualitative confirmation of the results (α is irrelevant on Pn below a certain Re , Pn increases as l/h decreases), a good quantitative agreement is found.

Figure 15 shows a comparison of the present mass transfer results with CFD results from [35] and experimental results from [36]. For the comparison of \overline{Sh} , it is assumed proportional to $Sc^{0.4}$ [40]. For $l/h4$ the agreement with the present results is good; for $l/h2$ the CFD results of Li et al. exhibit a strange tendency to become flat at low Re , and the agreement with our results is less satisfactory. On the whole, the effect of the parameters l/h and α is found to be qualitatively comparable.

Figure 16 reports a comparison between the present CFD results and the only data found in literature for woven spacers (experimental mass transfer results from [36]). In the narrow range of superposition ($Pn \approx 10^5$) the present CFD results overestimate slightly \overline{Sh} and overestimate the slope of the $\overline{Sh}-Pn$ curves; however, a similar influence of the flow attack angle α is shown; in fact, $\alpha45$ exhibits higher \overline{Sh} than $\alpha0$ and the two curves approach each other as Pn increases.

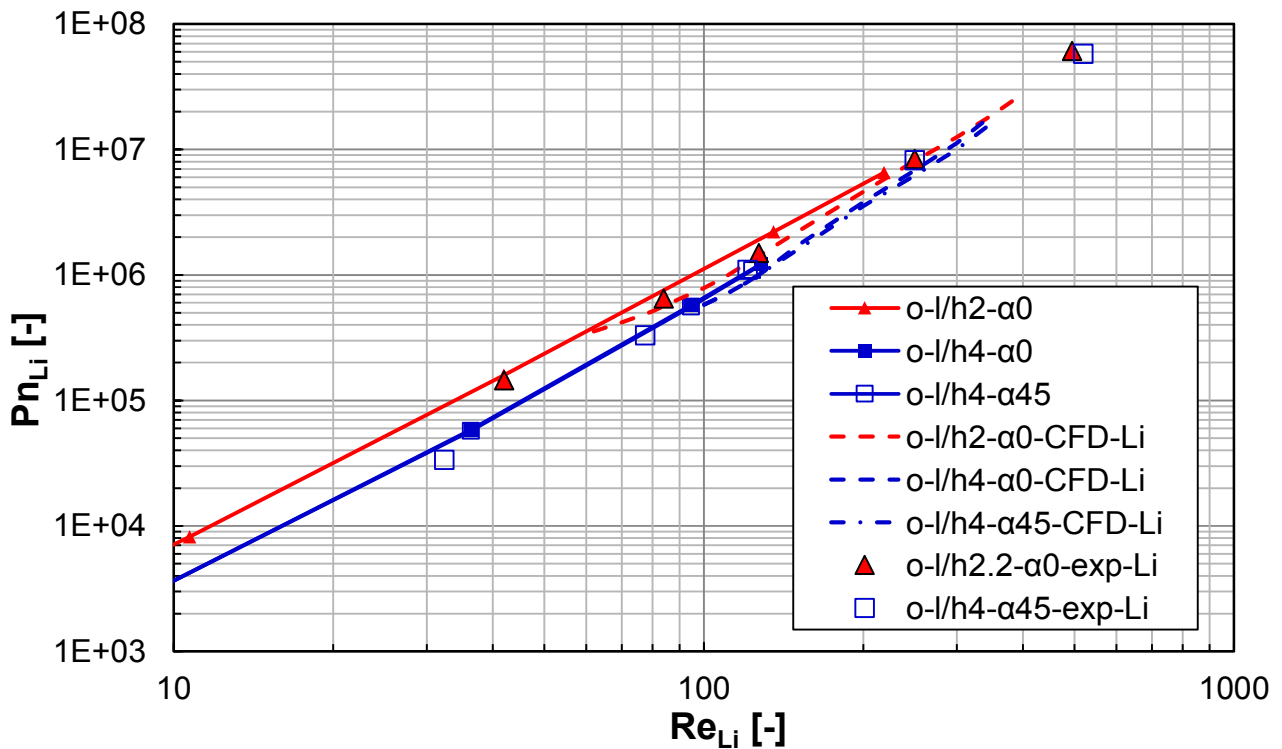


Figure 14. Power number as a function of Reynolds number for some cases simulated. Comparison with results of Li et al. [35] (CFD) and [36] (experimental).

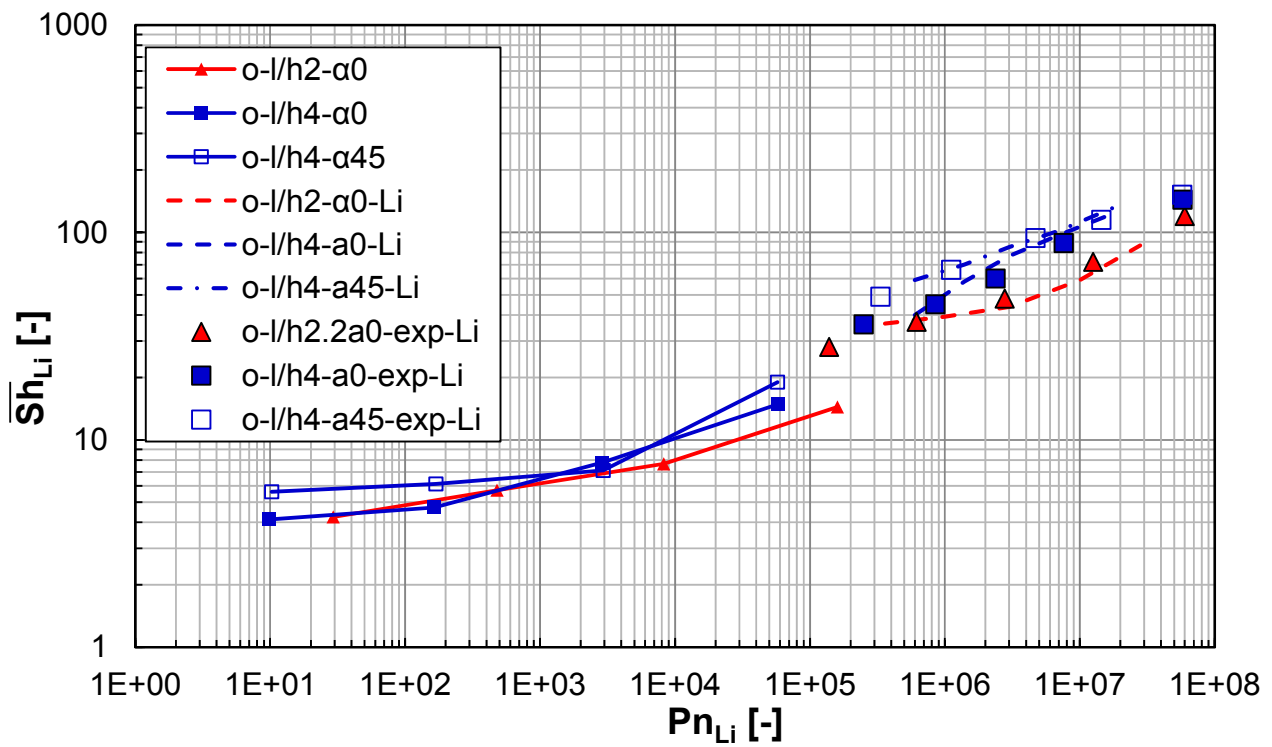


Figure 15. Sherwood number as a function of Power number for some cases simulated. Comparison with results of Li et al. [35] (CFD) and [36] (experimental).

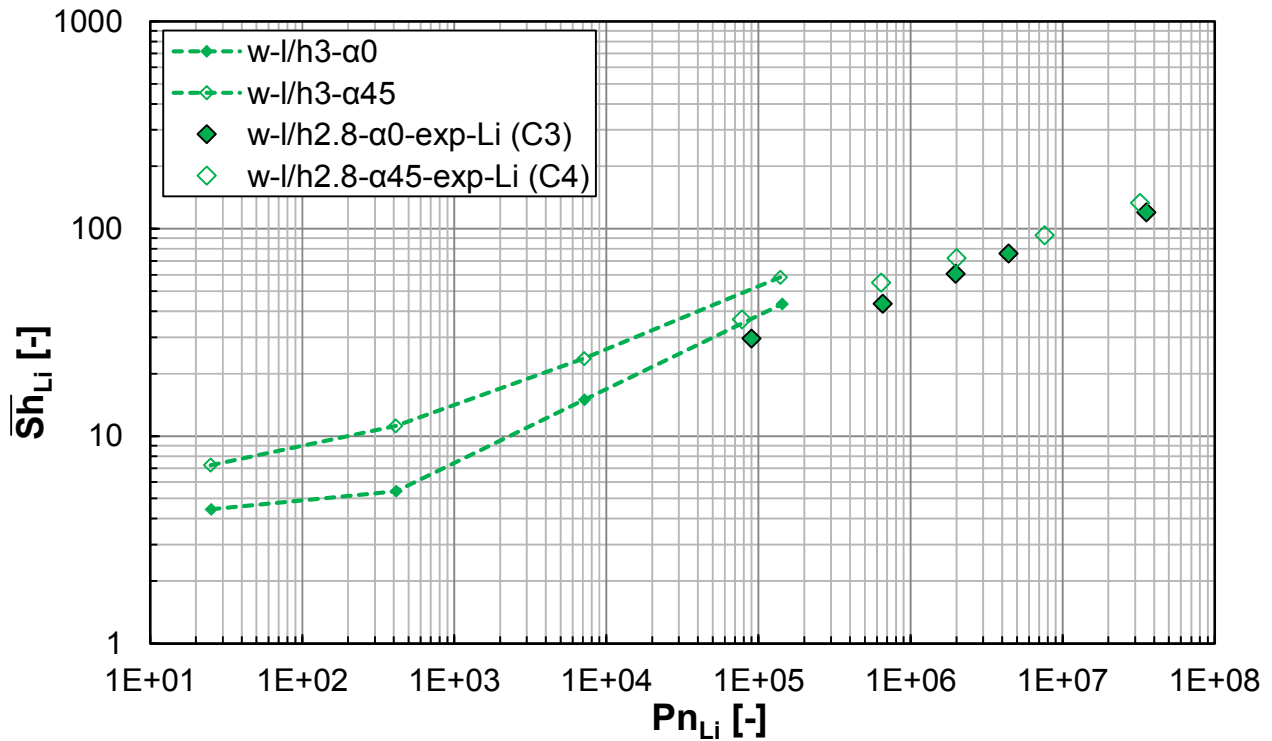


Figure 16. Sherwood number as a function of Power number for some cases simulated. Comparison with results of Li et al. [36] (experimental).

Another comparison was performed with the results of Koutsou et al. [39, 40], obtained by DNS CFD simulations and experiments. As a difference with respect to the present simulations, in the work by these authors one has $d = h/2$, the dependence of \overline{Sh} on Sc is studied, grid volumes are less ($\sim 300,000$ in [39] and from 540,000 to 1,000,000 in [40]), and the boundary condition at the walls is that of a fixed concentration. A spatially averaged value of the local time-averaged mass transfer coefficient k is calculated.

Figure 17 shows a comparison in terms of dimensionless pressure drop with DNS results and experimental data in [39]. Note that the simulations in [39] overestimate the hydraulic friction by up to $\sim 35\%$ with respect to the experimental results by the same authors. Conversely, a better agreement is found between the present CFD results and the experimental data of [39]; the highest discrepancy, $\sim 32\%$, is found at a Reynolds number of 37 for $l/h = 3$, where the experimental point appears to not follow the trend of the other points.

Figure 18 reports \overline{Sh} as a function of Re for the same cases as in Figure 17. CFD and experimental results from [40] are reported. In this case there is a gap which does not allow a direct comparison; however it is confirmed that the filament spacing does not affect strongly \overline{Sh} , and that the slope of the $\overline{Sh}-Re$ curves is similar to that predicted in the present work. Figure 18 shows also non-negligible discrepancies between the CFD results and the experimental data of Koutsou et al. [40].

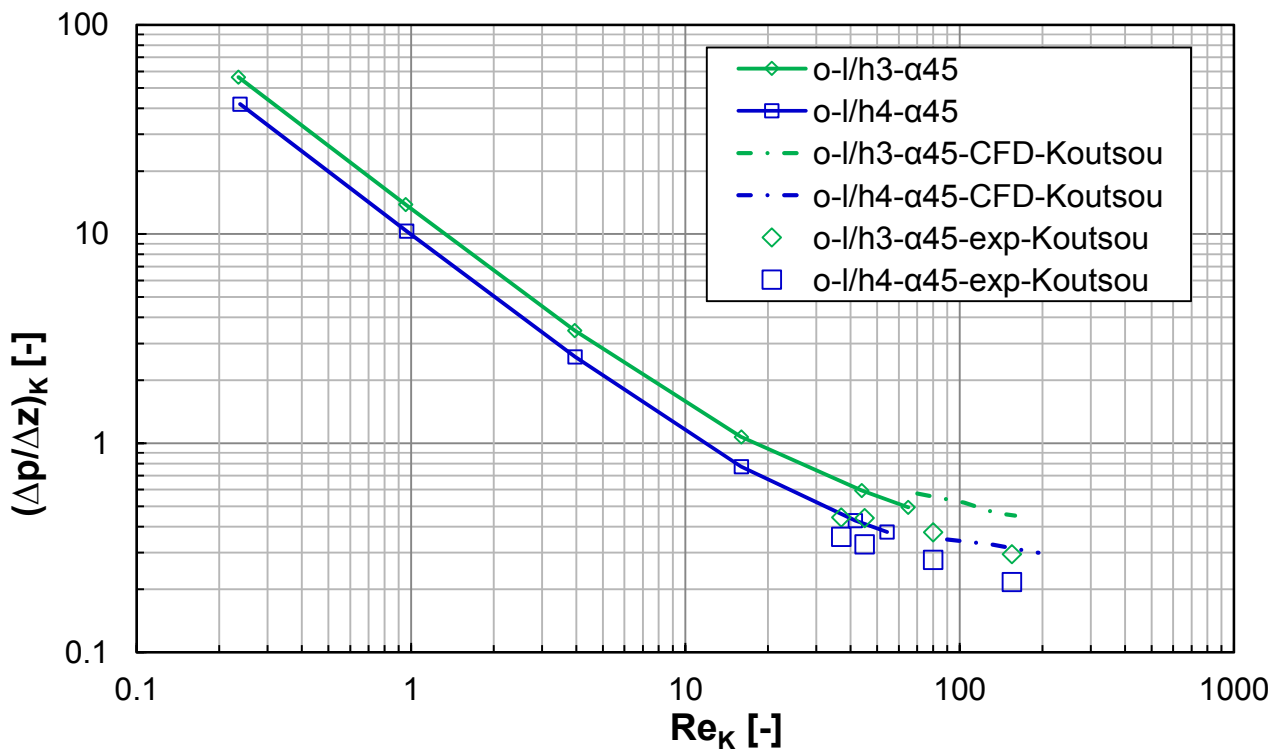


Figure 17. Dimensionless pressure drop as a function of Reynolds number for some cases simulated. Comparison with CFD and experimental results of Koutsou et al. [39].

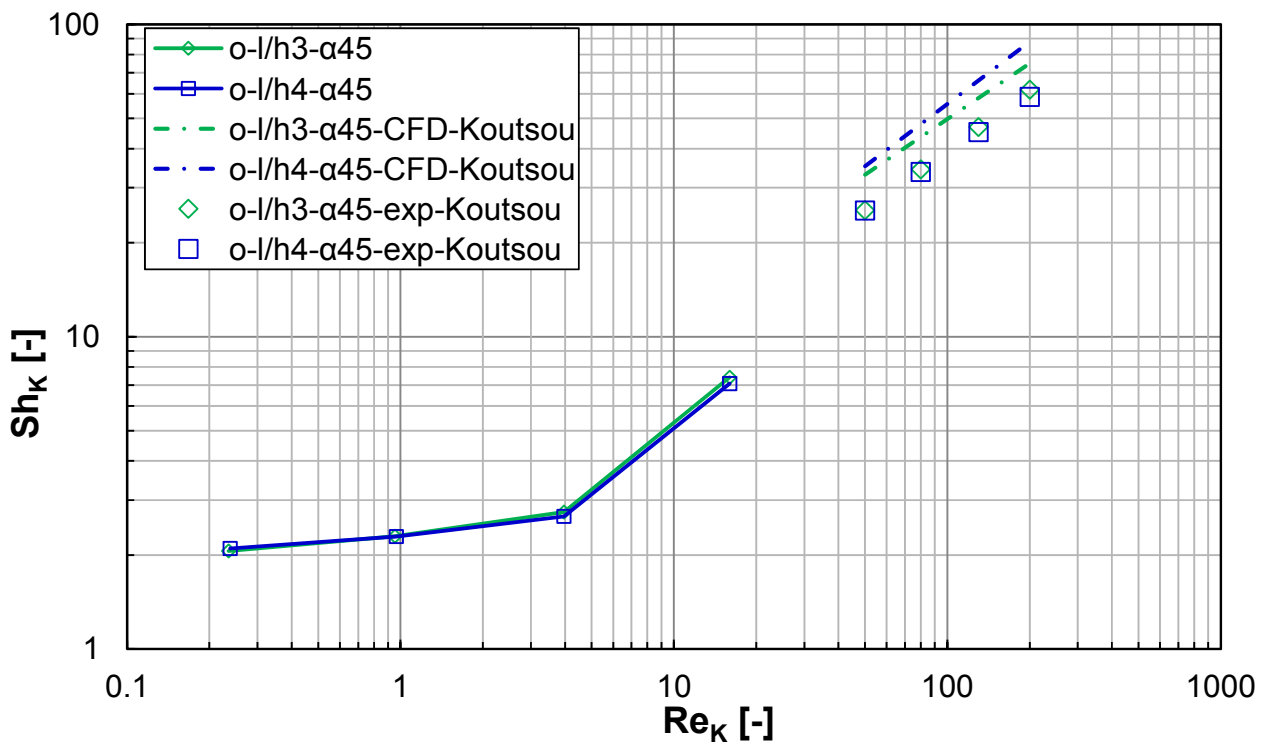


Figure 18. Sherwood number as a function of Reynolds number for some cases simulated. Comparison with CFD and experimental results of Koutsou et al. [40].

Another thorough CFD analysis of overlapped spacer-filled channels was presented by Shakaib et al. [41, 42]. In their papers, trends with Re are not shown, but only values at a fixed Re higher than the largest studied in the present work (64). Moreover, data are mostly reported in dimensional form without the indication of the channel height, so that no comparative charts can be presented here. However, further simulations were carried out and at higher Re and some relevant trends can be compared.

At $Re = 125$ (as defined in [42]) our prediction of the friction factor for the case $o-l/h4-\alpha0$ is higher by $\sim 7.6\%$ than that in [42]. The simulations in [41, 42] confirm that pressure drop increases as l/h decreases for all flow attack angles, while a slight effect of α is found. In particular, similar relative increments of pressure drop are found as in our simulations when l/h decreases. On the average for both attack angles, this increment is 33.0% in [42] vs. 31.6% in the present simulations going from $l/h4$ to $l/h3$, while it is 38.7% in [42] vs. 44.8% in the present simulations as one goes from $l/h3$ to $l/h2$. In regards to the attack angle, the agreement is less good: in [42] increments of 7.1% , 14.0% and 3.4% are reported from $\alpha0$ to $\alpha45$ for $l/h2$, $l/h3$ and $l/h4$ respectively, while they amount to -4.0% , 9.0% , -2.4% in the present simulations.

Ref. [42] reports also mass transfer coefficients. These confirm that (i) the angle $\alpha45$ enhances mass transfer for all l/h values with respect to $\alpha0$ (in the present simulations the same effect is found for all Re apart from $Re = 16$), and (ii) for $\alpha45$ the ranking of mass transfer coefficients is $l/h3 > l/h4 > l/h2$, as was found in the present simulations at the highest Re investigated of 64.

4 Conclusions

CFD simulations of fluid flow and mass transfer in spacer-filled channels for reverse electro dialysis were carried out. The effect of the spacer configuration was assessed in a parametric analysis, where woven (w) and non-woven (o , overlapped) spacers with crossing filaments arranged

at 90° were simulated, with three pitch to height ratios ($l/h = 2, 3, 4$), two different flow directions (parallel to a filament, i.e. $\alpha 0$, and bisecting the angle formed by the filaments, i.e. $\alpha 45$) and four Reynolds numbers (1, 4, 16, 64).

The flow was found to be steady in all cases. The presence of a spacer causes velocity components perpendicular to the main flow direction, but calm regions with low fluid velocities and poor mixing are generated in the proximity of the filaments. Only in the case $w-\alpha 45$ the filaments do not cause this drawback.

At low Re creeping flow conditions are observed. As Re increases, increasing inertial effects arise, and a secondary flow develops, so that the flow field loses self-similarity, and a mixing enhancement is obtained. However, the friction coefficient remains approximately proportional to Re^{-1} and therefore the specific power consumption remains approximately proportional to Re^2 . Pn values from ~ 3 to ~ 20 times higher than in the void channel are obtained; these increments increase slightly as Re increases. Spacers provide a mass transfer enhancement with respect to the empty channel only beyond a specific cut-off value of Re , while at very low Re they act mainly as resistances hindering mass transfer. In the case $w-\alpha 45$ this cut-off Re is lower than 1, in the other cases it is higher, but, however, less than ~ 7 . As Re increases, Sh values much higher than in the void channel are attained. All parameters affect the distribution of the local Sherwood number on the walls, but, among them, filament arrangement (w/o) and α ($0^\circ / 45^\circ$) are the most important ones.

More in detail, the effects of the various parameters can be summarized as follows:

- As l/h decreases, the streamlines are more curved on the average and Pn increases, especially for the w -arrangement (increments up to 210% from $w-l/h4$ to $w-l/h2$). The filament spacing has a clear effect on \overline{Sh} for all Re only in the case $w-\alpha 45$; in particular, \overline{Sh} decreases as l/h increases. For $w-\alpha 0$ this occurs only at the highest Re . For the o -arrangement the dependence of \overline{Sh} on l/h is not significant.

- The filament arrangement is a key parameter. The w -arrangement establishes flow fields fully different from those typical of the overlapped one, raising pressure drop, but favouring mixing especially for higher Reynolds numbers and $\alpha = 45^\circ$ (Sherwood numbers up to ~ 6.5 times higher). Notably, the influence is larger as the pitch decreases: w -spacers yield Pn higher on the average by 106%, 67% and 54% with respect to the o -spacers, for $l/h = 2, 3, 4$ respectively. The effect of the filament arrangement is due to the fact that woven wires exhibit larger surface area for friction, larger velocity gradients at the walls and larger inertial effects.
- The flow attack angle α influences deeply the flow field. In the case $o-\alpha 0$ the lateral motion is confined inside the unit cell, while in the case $o-\alpha 45$ some fluid threads follow the filaments and thus remain in the half-channel of entry, while some fluid threads move into the opposite half-channel along 3D zigzag flow paths, with a predominance of the former when l/h decreases and Re increases. For the w -arrangement the streamlines present a rectilinear part at low Re and high l/h , but the case $w-\alpha 45$ shows more displacements in the lateral direction and the absence of stagnant areas with respect to the case $w-\alpha 0$. This is a prominent feature which makes the case $w-\alpha 45$ the most promising configuration for mixing. The configuration $w-\alpha 45$ implies \overline{Sh} higher than the case $w-\alpha 0$ for all Re and l/h , but the discrepancies are lower at high Re . For the o -arrangement the effect of α is less marked but more complex than in the w -arrangement as Re varies. However, α does not significantly affect pressure drop for both filament arrangements, probably because viscous stresses are predominant with respect to the inertial ones in the range investigated.

The $\overline{Sh}-Pn$ trends are qualitatively the same as the $\overline{Sh}-Re$ ones. As a difference, the pitch has no significant effect for the configuration $w-\alpha 0$, especially at high Pn ; for the o -arrangement the dependence of \overline{Sh} on l/h is still small, but it increases at high Pn .

Finally, a satisfactory agreement is found with the literature, although the comparison is not easy due (i) to the different ranges of Re investigated, (ii) to the presence of very few data on woven spacers and (iii) to the discrepancies observed among the various studies.

The present results show that the spacer features have a strong impact on process performance. For all Re and all Pn , the highest \overline{Sh} values are obtained by the configuration $w-l/h2-\alpha45$. The woven spacers, poorly investigated up to now, are very promising: mixing is enhanced by complex flow fields with significant vertical and lateral motions, especially for the case $w-\alpha45$ where calm regions are absent. Therefore proper attention should be paid to them in the choice of the spacer configuration. Notably, the performance evaluation of spacers in RED stacks should take into account other factors, besides Pn and Sh . Residence time, electrical resistance, solutions adopted, channel deformation, spacer shadow effect, and the actual size of the spacer-filled channels also affect the net producible power. Thus, the simulation results should be used as input data for a process simulator, in order to find the optimal channel configuration and operative conditions.

Acknowledgement

This work has been performed within the REAPower (Reverse Electrodialysis Alternative Power production) project, funded by the EU-FP7 programme (Project Number: 256736), <http://www.reapower.eu>.

Notation

$\Delta p/\Delta z$	Mean pressure gradient along the main flow direction [Pa m ⁻¹]
A	Coefficient in Eq. (20) [-]
a	Slope of the function $\rho(C)$ obtained via linear regression [kg mol ⁻¹]
B	Coefficient in Eq. (21) [-]
b	Intercept of the function $\rho(C)$ obtained via linear regression [kg m ⁻³]

C	Molar concentration of electrolyte [mol m^{-3}]
\tilde{C}	Periodic molar concentration of electrolyte [mol m^{-3}]
\hat{C}_b	Bulk concentration of electrolyte [mol m^{-3}]
C_w	Local molar concentration of electrolyte in the membrane-solution interfaces [mol m^{-3}]
\bar{C}_w	Mean molar concentration of electrolyte in the membrane-solution interfaces [mol m^{-3}]
D	Measured diffusion coefficient of electrolyte [$\text{m}^2 \text{s}^{-1}$]
D_{corr}	Corrected diffusion coefficient [m s^{-2}]
$D_{corr,ave}$	Average corrected diffusion coefficient [m s^{-2}]
d	Filament diameter [m]
$d_{h,void}$	Hydraulic diameter of the spacer-less channel [m]
F	Faraday's constant [C mol^{-1}]
f	Fanning friction factor [-]
h	Channel thickness [m]
i	Current density [A m^{-2}]
J_{IEM}^d	Diffusive flux of electrolyte at the membrane-solution interface [$\text{mol m}^{-2} \text{s}^{-1}$]
\bar{J}_{IEM}^d	Mean diffusive flux at the membranes-solution interface [$\text{mol m}^{-2} \text{s}^{-1}$]
K_c	Concentration gradient along the main flow direction [mol m^{-4}]
k	Mass transfer coefficient [m s^{-1}]
\bar{k}	Average mass transfer coefficient [m s^{-1}]
l	Mesh length [m]
M_e	Molar mass of electrolyte [kg mol^{-1}]
m	Exponent to Re for f in Eq. (21) [-]
n	Exponent to Re for Pn in Eq. (20) [-]
\bar{P}	Body force per unit volume [Pa m^{-1}]
Pn	Power number
p	Pressure [Pa]
\tilde{p}	Periodic component of pressure [Pa]
Re	Reynolds number [-]
S	Area of membrane-solution interfaces [m^2]
Sc	Schmidt number [-]
Sh	Sherwood number [-]
\bar{Sh}	Average Sherwood number [-]
SPC	Specific power consumption [Pa s^{-1}]
t	Time [s]
\vec{u}	Velocity of solution [m s^{-1}]
u_{norm}	Normalized velocity, $ \vec{u} /w_{ave}$ [-]
V	Volume of a Unit Cell [m^3]

w	Velocity component along the flow direction z [m s^{-1}]
w_{ave}	Average velocity along z in the unit cell [m s^{-1}]
$w_{mean,void}$	Average velocity along z in a corresponding spacerless channel [m s^{-1}]
x	Cartesian position coordinate [m]
y	Cartesian position coordinate [m]
z	Cartesian position coordinate [m]

Greek letters

α	Flow attack angle [$^{\circ}$]
μ	Dynamic viscosity of solution [Pa s]
ρ	Solution density [kg m^{-3}]

Abbreviations

<i>CFD</i>	Computational Fluid Dynamics
<i>DNS</i>	Direct Numerical Simulation
<i>RED</i>	Reverse ElectroDialysis

References

- [1] P. Długołęcki, K. Nijmeijer, S.J. Metz, M. Wessling, Current status of ion exchange membranes for power generation from salinity gradients, *J. Membr. Sci.*, 319 (2008) 214-222.
- [2] L. Gurreri, A. Tamburini, A. Cipollina, G. Micale, M. Ciofalo, CFD prediction of concentration polarization phenomena in spacer-filled channels for reverse electrodialysis, *J. Membr. Sci.*, 468 (2014) 133-148.
- [3] R.E. Pattle, Production of electric power by mixing fresh and salt water in hydroelectric pile, *Nature*, 174 (1954) 660.
- [4] J.W. Post, H.V.M. Hamelers, C.J.N. Buisman, Energy recovery from controlled mixing salt and fresh water with a reverse electrodialysis system, *Environ. Sci. Technol.*, 42 (2008) 5785-5790.
- [5] J. Veerman, M. Saakes, S.J. Metz, G.J. Harmsen, Reverse electrodialysis: Performance of a stack with 50 cells on the mixing of sea and river water, *J. Membr. Sci.*, 327 (2009) 136-144.
- [6] A. Cipollina, F. Giacalone, F. Grisafi, G. Micale, A. Tamburini, G. Vella, Lab-scale investigation of a Pressure Retarded Osmosis module fed by salinity gradients, *Desalin. Water Treat.*, (accepted for publication, 2015).

- [7] P. Długołęcki, P. Ogonowski, S.J. Metz, M. Saakes, K. Nijmeijer, M. Wessling, On the resistances of membrane, diffusion boundary layer and double layer in ion exchange membrane transport, *J. Membr. Sci.*, 349 (2010) 369-379.
- [8] V. Geraldes, V. Semião, M.N. Pinho, Hydrodynamics and concentration polarization in NF/RO spiral-wound modules with ladder-type spacers, *Desalination*, 157 (2003) 395-402.
- [9] Y. Kim, W.S. Walker, D.F. Lawler, Electrodialysis with spacers: Effects of variation and correlation of boundary layer thickness, *Desalination*, 274 (2011) 54-63.
- [10] H.-J. Lee, H. Strathmann, S.-H. Moon, Determination of the limiting current density in electrodialysis desalination as an empirical function of linear velocity, *Desalination*, 190 (2006) 43-50.
- [11] E. Nagy, E. Kulcsára, A. Nagy, Membrane mass transport by nanofiltration: Coupled effect of the polarization and membrane layers, *J. Membr. Sci.*, 368 (2011) 215-222.
- [12] S.S. Sablani, M.F.A. Goosen, R. Al-Belushi, M. Wilf, Concentration polarization in ultrafiltration and reverse osmosis: a critical review, *Desalination*, 141 (2001) 269-289.
- [13] H. Strathmann, Electrodialysis, a mature technology with a multitude of new applications, *Desalination*, 264 (2010) 268-288.
- [14] A. Tamburini, A. Cipollina, S. Al-Sharif, M. Albeirrutty, L. Gurreri, G. Micale, M. Ciofalo, Assessment of temperature polarization in membrane distillation channels by liquid crystal thermography, *Desalin. Water Treat.*, 55 (2015) 2747-2765.
- [15] Y. Tanaka, Pressure distribution, hydrodynamics, mass transport and solution leakage in an ion-exchange membrane electro dialyzer, *J. Membr. Sci.*, 234 (2004) 23-39.
- [16] M. Tedesco, A. Cipollina, A. Tamburini, I.D.L. Bogle, G. Micale, A simulation tool for analysis and design of Reverse Electrodialysis using concentrated brines, *Chem. Eng. Res. Des.*, 93 (2015) 441-456.
- [17] D.A. Vermaas, E. Guler, M. Saakes, K. Nijmeijer, Theoretical power density from salinity gradients using reverse electrodialysis, *Energy Procedia*, 20 (2012) 170-184.
- [18] H. Strathmann, Ion-exchange membrane separation processes, first ed., Elsevier, Amsterdam, 2004.
- [19] D.A. Vermaas, M. Saakes, K. Nijmeijer, Doubled power density from salinity gradients at reduced intermembrane distance, *Environ. Sci. Technol.*, 45 (2011) 7089-7095.
- [20] M. Bevacqua, A. Carubia, A. Cipollina, A. Tamburini, M. Tedesco, G. Micale, Performance of a RED system with Ammonium Hydrogen Carbonate solutions, *Desalin. Water Treat.*, (accepted for publication, 2015).
- [21] R.E. Lacey, Energy by reverse electrodialysis, *Ocean Eng.*, 7 (1980) 1-47.

- [22] J. Veerman, M. Saakes, S.J. Metz, G.J. Harmsen, Electrical power from sea and river water by reverse electrodialysis: a first step from the laboratory to a real power plant, *Environ. Sci. Technol.*, 44 (2010) 9207-9212.
- [23] D.A. Vermaas, M. Saakes, K. Nijmeijer, Power generation using profiled membranes in reverse electrodialysis, *J. Membr. Sci.*, 385-386 (2011) 234-242.
- [24] D.A. Vermaas, M. Saakes, K. Nijmeijer, Enhanced mixing in the diffusive boundary layer for energy generation in reverse electrodialysis, *J. Membr. Sci.*, 453 (2014) 312-319.
- [25] J. Jagur-Grodzinski, R. Kramer, Novel process for direct conversion of free energy of mixing into electric power, *Ind. Eng. Chem. Process Des. Dev.*, 25 (1986) 443-449.
- [26] J. Veerman, M. Saakes, S.J. Metz, G.J. Harmsen, Reverse electrodialysis: A validated process model for design and optimization, *Chem. Eng. J.*, 166 (2011) 256-268.
- [27] M.S. Isaacson, A.A. Sonin, Sherwood number and friction factor correlations for electrodialysis systems, with application to process optimization, *Ind. Eng. Chem. Proc. Dd.*, 15 (1976) 313-321.
- [28] Y. Tanaka, Limiting current density of an ion-exchange membrane and of an electrodialyzer, *J. Membr. Sci.*, 266 (2005) 6-17.
- [29] J. Balster, I. Pünt, D.F. Stamatialis, M. Wessling, Multi-layer spacer geometries with improved mass transport, *J. Membr. Sci.*, 282 (2006) 351-361.
- [30] G. Schock, A. Miquel, Mass transfer and pressure loss in spiral wound modules, *Desalination*, 64 (1987) 339-352.
- [31] A.R. Da Costa, A.G. Fane, D.E. Wiley, Spacer characterization and pressure drop modelling in spacer filled channel for ultrafiltration, *J. Membr. Sci.*, 87 (1994) 79-98.
- [32] J. Schwinge, D.E. Wiley, D.F. Fletcher, Simulation of the flow around spacer filaments between channel walls. 1. Hydrodynamics, *Ind. Eng. Chem. Res.*, 41 (2002) 2977-2987.
- [33] J. Schwinge, D.E. Wiley, D.F. Fletcher, Simulation of the flow around spacer filaments between channel walls. 2. Mass-Transfer Enhancement, *Ind. Eng. Chem. Res.*, 41 (2002) 4879-4888.
- [34] S.K. Karode, A. Kumar, Flow visualization through spacer filled channels by computational fluid dynamics I. Pressure drop and shear rate calculations for flat sheet geometry, *J. Membr. Sci.*, 193 (2001) 69-84.
- [35] F. Li, W. Meindersma, A.B. de Haan, T. Reith, Optimization of commercial net spacers in spiral wound membrane modules, *J. Membr. Sci.*, 208 (2002) 289-302.
- [36] F. Li, W. Meindersma, A.B. de Haan, T. Reith, Experimental validation of CFD mass transfer simulations in flat channels with non-woven net spacers, *J. Membr. Sci.*, 232 (2004) 19-30.

- [37] V.V. Ranade, A. Kumar, Fluid dynamics of spacer filled rectangular and curvilinear channels, *J. Membr. Sci.*, 271 (2006) 1-15.
- [38] L.C. Santos, V. Geraldés, S. Velizarov, J.G. Crespo, Investigation of flow patterns and mass transfer in membrane module channels filled with flow-aligned spacers using computational fluid dynamics (CFD), *J. Membr. Sci.*, 305 (2007) 103-117.
- [39] C.P. Koutsou, S.G. Yiantsios, A.J. Karabelas, Direct numerical simulation of flow in spacer-filled channels: Effect of spacer geometrical characteristics, *J. Membr. Sci.*, 291 (2007) 53-69.
- [40] C.P. Koutsou, S.G. Yiantsios, A.J. Karabelas, A numerical and experimental study of mass transfer in spacer-filled channels: Effects of spacer geometrical characteristics and Schmidt number, *J. Membr. Sci.*, 326 (2009) 234-251.
- [41] M. Shakaib, S.M.F. Hasani, M. Mahmood, Study on the effects of spacer geometry in membrane feed channels using three-dimensional computational flow modeling, *J. Membr. Sci.*, 297 (2007) 74-89.
- [42] M. Shakaib, S.M.F. Hasani, M. Mahmood, CFD modeling for flow and mass transfer in spacer-obstructed membrane feed channels, *J. Membr. Sci.*, 326 (2009) 270-284.
- [43] S.M. Mojab, A. Pollard, J.G. Pharoah, S.B. Beale, E.S. Hanff, Unsteady laminar to turbulent flow in a spacer-filled channel, *Flow turbul. combust.*, 92 (2014) 563-577.
- [44] J. Schwinge, D.E. Wiley, D.F. Fletcher, A CFD study of unsteady flow in narrow spacer-filled channels for spiral-wound membrane modules, *Desalination*, 146 (2002) 195-201.
- [45] D. Dendukuri, S.K. Karode, A. Kumar, Flow visualization through spacer filled channels by computational fluid dynamics-II: Improved feed spacer designs, *J. Membr. Sci.*, 249 (2005) 41-49.
- [46] F. Li, W. Meindersma, A.B. de Haan, T. Reith, Novel spacers for mass transfer enhancement in membrane separations, *J. Membr. Sci.*, 253 (2005) 1-12.
- [47] J. Schwinge, D.E. Wiley, A.G. Fane, Novel spacer design improves observed flux, *J. Membr. Sci.*, 229 (2004) 53-61.
- [48] A. Shrivastava, S. Kumar, E.L. Cussler, Predicting the effect of membrane spacers on mass transfer, *J. Membr. Sci.*, 323 (2008) 247-256.
- [49] P. Xie, L.C. Murdoch, D.A. Ladner, Hydrodynamics of sinusoidal spacers for improved reverse osmosis performance, *J. Membr. Sci.*, 453 (2014) 92-99.
- [50] S. Wardeh, H.P. Morvan, CFD simulations of flow and concentration polarization in spacer-filled channels for application to water desalination, *Chem. Eng. Res. Des.*, 86 (2008) 1107-1116.
- [51] D.E. Wiley, D.F. Fletcher, Computational fluid dynamics modelling of flow and permeation for pressure-driven membrane processes, *Desalination*, 145 (2002) 183-186.

- [52] D.E. Wiley, D.F. Fletcher, Techniques for computational fluid dynamics modeling of flow in membrane channels, *J. Membr. Sci.*, 211 (2003) 127-137.
- [53] A. Tamburini, G. Micale, M. Ciofalo, A. Cipollina, Experimental analysis via Thermochromic Liquid Crystals of the temperature local distribution in Membrane Distillation modules, *Chem. Eng. Trans.*, 32 (2013) 2041-2046.
- [54] A. Tamburini, P. Pitò, A. Cipollina, G. Micale, M. Ciofalo, A Thermochromic Liquid Crystals image analysis technique to investigate temperature polarization in spacer-filled channels for membrane distillation, *J. Membr. Sci.*, 447 (2013) 260-273.
- [55] A. Daniilidis, D.A. Vermaas, R. Herber, K. Nijmeijer, Experimentally obtainable energy from mixing river water, seawater or brines with reverse electrodialysis, *Renew. Energy*, 64 (2014) 123-131.
- [56] P. Długolecki, A. Gambier, K. Nijmeijer, M. M. Wessling, Practical potential of reverse electrodialysis as process for sustainable energy generation, *Environ. Sci. Technol.*, 43 (2009) 6888-6894.
- [57] D.W. Green, R.H. Perry, *Perry's Chemical Engineers' Handbook*, eighth ed., McGraw-Hill, New York, 2007.
- [58] H. Ozbek, J.A. Fair, S.L. Phillips, *Viscosity of aqueous sodium chloride solutions from 0 - 150°C*, University of California, Berkeley, 2010.
- [59] V. Vitagliano, P.A. Lyons, Diffusion coefficients for aqueous solutions of sodium chloride and barium chloride, *J. Am. Chem. Soc.*, 78 (1956) 1549-1552.
- [60] E. Brauns, Towards a worldwide sustainable and simultaneous large-scale production of renewable energy and potable water through salinity gradient power by combining reversal electrodialysis and solar power?, *Desalination*, 219 (2008) 312-323.
- [61] E. Brauns, An alternative hybrid concept combining seawater desalination, solar energy and reverse electrodialysis for a sustainable production of sweet water and electrical energy, *Desalin. Water Treat.*, 13 (2010) 53-62.
- [62] M. Tedesco, A. Cipollina, A. Tamburini, G. Micale, J. Helsen, M. Papapetrou, Reapower - Use of desalination brine for power production through reverse electrodialysis, *Desalin. Water Treat.*, 53 (2015).
- [63] L. Gurreri, M. Ciofalo, A. Cipollina, A. Tamburini, W. van Baak, G. Micale, CFD modelling of profiled-membrane channels for Reverse Electrodialysis, *Desalin. Water Treat.*, 55 (2015) 3404-3423.
- [64] L. Gurreri, *Computational fluid dynamics of reverse electrodialysis systems*, PhD thesis, Dipartimento di Ingegneria Chimica, Gestionale, Informatica, Meccanica, Università degli Studi di Palermo, 2015.

- [65] A. Tamburini, G. La Barbera, A. Cipollina, M. Ciofalo, G. Micale, CFD simulation of channels for direct and reverse electrodialysis, *Desalin. Water Treat.*, 48 (2012) 370-389.
- [66] L. Gurreri, A. Tamburini, A. Cipollina, G. Micale, CFD analysis of the fluid flow behavior in a reverse electrodialysis stack, *Desalin. Water Treat.*, 48 (2012) 390-403.
- [67] Y.L. Li, K.L. Tung, CFD simulation of fluid flow through spacer-filled membrane module: selecting suitable cell types for periodic boundary conditions, *Desalination*, 233 (2008) 351-358.
- [68] A. Tamburini, G. La Barbera, A. Cipollina, G. Micale, M. Ciofalo, CFD prediction of scalar transport in thin channels for reverse electrodialysis, *Desalin. Water Treat.*, in press, DOI: 10.1080/19443994.2014.959735 (2014).
- [69] G.A. Fimbres-Weihs, D.E. Wiley, Numerical study of two-dimensional multi-layer spacer designs for minimum drag and maximum mass transfer, *J. Membr. Sci.*, 325 (2008) 809-822.